Journal of Geophysical Research: Atmospheres

RESEARCH ARTICLE
10.1029/2018JD028696

A Lagrangian Model Diagnosis of Stratospheric Contributions to Tropical Midtropospheric Air

M. Tao[1], L. L. Pan[2], P. Konopka[1], S. B. Honomichl[2], D. E. Kinnison[2], and E. C. Apel[2]

[1]Forschungszentrum Jülich (IEK-7: Stratosphere), Jülich, Germany, [2]National Center for Atmospheric Research, Boulder, CO, USA

Key Points:
- Processes contributing to the observed O_3 enhancement in the tropical midtroposphere are diagnosed using a Lagrangian transport model
- The leading process is found to be transport from the stratosphere via isentropic mixing across the subtropical jet
- Biomass burning facilitated O_3 production is also identified by correlations among O_3, HCN, and CO for a fraction of the observations

Supporting Information:
- Supporting Information S1
- Movie S1

Correspondence to:
M. Tao,
m.tao@fz-juelich.de

Citation:
Tao, M., Pan, L. L., Konopka, P., Honomichl, S. B., Kinnison, D. E., & Apel, E. C. (2018). A Lagrangian model diagnosis of stratospheric contributions to tropical midtropospheric air. *Journal of Geophysical Research: Atmospheres*, *123*, 9764–9785. https://doi.org/10.1029/2018JD028696

Received 22 MAR 2018
Accepted 12 JUL 2018
Accepted article online 28 JUL 2018
Published online 3 SEP 2018

Abstract Airborne in situ observations during the Convective Transport of Active Species in the Tropics campaign in January–February 2014 revealed a large region over the tropical western Pacific where the midtroposphere had a layered structure with a distinct chemical signature of high ozone and low water vapor (HOLW). The observed anticorrelation between ozone and water vapor is a strong indication of transport from the midlatitude upper troposphere and lower stratosphere. This work presents a diagnosis of stratospheric air in the tropical western Pacific midtroposphere through isentropic transport and mixing. Using the Chemical Lagrangian Model of the Stratosphere, we characterize and quantify the contribution of transported stratospheric air to the observed HOLW layers. The result indicates that the isentropic transport is an effective process for stratospheric air to mix into the tropical midtroposphere. Using the modeled stratospheric tracer and 3-D back trajectories, we identified that 60% of the observed HOLW air masses contain significant stratospheric influence. We have also examined possible contribution to the HOLW layer from ozone production related to biomass burning emissions. Clear chemical signature of this process is found in ~8% of the HOLW air masses, identified by positive correlations among O_3, HCN, and CO. This analysis provides the first quantitative diagnosis of the contribution from the stratosphere-to-troposphere transport, highlights the importance of mixing in chemical transport, and demonstrates the limitations of pure Lagrangian trajectory calculations in quantifying transport.

1. Introduction

Tropospheric ozone (O_3) plays an important role in both atmospheric chemistry and chemistry-climate interactions. As a precursor for hydroxyl, O_3 in part controls atmospheric oxidation capacity (Brasseur et al., 1999; Nicely et al., 2016; Rex et al., 2014). As a greenhouse gas, tropospheric O_3 is one of the most important short-lived climate forcers (e.g., Monks et al., 2015; Shindell & Faluvegi, 2009; Stevenson et al., 2013; Stocker, 2014). Tropospheric O_3 varies over a wide range of spatial and temporal scales due to variability of both anthropogenic emissions and the atmospheric circulation (Cooper et al., 2014). Understanding the controlling mechanisms of tropospheric O_3 requires integrated studies of both observations and modeling. Tropospheric O_3 generally shows a relatively low concentration in the tropics, especially over the region of tropical oceans where deep convection is persistent (Oltmans et al., 2001; Thompson et al., 2011). However, numerous observational studies have revealed enhanced O_3 layers in the tropical midtroposphere [see, e.g., in Gregory et al. (1999) and Thouret et al. (2001) for the NASA Pacific Exploratory Mission (PEM) experiments and Newell et al. (1999) for the Measurement of Ozone and Water Vapor by Airbus In-Service Aircraft (MOZAIC) program).

Observations from a recent field campaign CONTRAST (Convective Transport of Active Species in the Tropics), conducted from Guam (13.5°N,144.8°E) during January–February 2014, found persistent midtropospheric layers with elevated ozone mixing ratio over the tropical western Pacific (TWP; Pan et al., 2017). According to CONTRAST measurements, the thin layers with elevated O_3 mainly occurred between 4 and 8 km (~320- to 340-K potential temperature). The ozone mixing ratios within these layers were between ~40 and 90 ppb, which is significantly elevated from the typical tropical tropospheric background value of ~20 ppb. These air masses are also drier, associated with low relative humidity (RH < 45%). Using O_3 and RH criteria, the middle tropospheric O_3 observations were identified to have a bimodal distribution: the background tropospheric air containing low ozone and high water vapor (LOHW) form a *primary mode*, and the O_3 elevated layers form a *secondary mode* (Pan et al., 2015) containing high O_3 and low H_2O (HOLW; Anderson et al., 2016).

Although the HOLW layers were reported in a series of previous observations (Hayashi et al., 2008; Newell et al., 1999; Thouret et al., 2001), the analysis of CONTRAST data revealed this bimodal behavior.

A well-recognized mechanism of ozone enhancements in the tropics is connected to biomass burning (BB) emissions of ozone precursors and its subsequent photochemical production. Oltmans et al. (2001) reported midtropospheric ozone enhancements in Southern Hemisphere Additional Ozonesonde (SHADOZ) observations and related it to the BB occurring in Australia and South America. Other in situ ozone measurements over the tropical Pacific revealed the importance of long-range transport of plumes influenced by BB in Indonesia (e.g., Kita et al., 2002; Kondo et al., 2002; Singh et al., 2000).

Using back trajectory analysis, Anderson et al. (2016) concluded that photochemically produced O_3 due to BB transported from central Africa and southeast Asia was the dominant process for the observed ozone enhancement during CONTRAST. The associated low RH was attributed to subsidence dehydration during the transport. However, there are questions as to whether BB-facilitated ozone production alone can explain the observations, considering the low production rate of ~2 ppbv/day (Jaffe & Wigder, 2012; Kondo et al., 2002) and the lack of direct measurements for the precursors required in the chemical reaction within the transported plumes.

An additional mechanism to produce layered tropical elevated ozone layers is equatorward and downward transport of midlatitude upper tropospheric and lower stratospheric (UTLS) air. A number of studies have attributed the frequent occurrences of HOLW structures in the subtropics and extratropics to stratosphere-troposphere exchange (STE; e.g., Hayashi et al., 2008). This transport process is considered to be the main mechanism for producing the observed extremely dry layer (*dry intrusions*) over the TWP during TOGA COARE in association with midlatitude air descending into the TWP (Mapes & Zuidema, 1996; Parsons et al., 1994; Yoneyama & Parsons, 1999). Cau et al. (2007) emphasized the role of extratropical baroclinic systems, the subtropical anticyclone variability, and Rossby wave breaking (RWB) by analyzing back trajectories.

Based on observed ozone and water vapor relationships during CONTRAST and the other mentioned studies, Pan et al. (2015) suggested that large-scale transport and mixing across the subtropical jet may be a significant contributor to the observed secondary mode. Randel et al. (2016) studied the climatological behavior of dry layers (RH < 20%) using CONTRAST data and Global Forecast System (GFS) analysis data and attributed the formation of *dry layers* mainly to quasi-isentropic transport from the extratropical UTLS.

The goal of this study is to quantitatively estimate the stratospheric influence on observed tropical midtropospheric air during the CONTRAST campaign. Previous works relating midtropospheric O_3 enhancement to STE primarily focused on the analysis of high-PV signatures (e.g., Postel & Hitchman, 1999; Waugh & Polvani, 2000) or back trajectories (e.g., Hayashi et al., 2008; Yoneyama & Parsons, 1999). In this work, we explore the process of mixing stratospheric air into the deep tropics beyond what can be identified by PV signatures or by pure back trajectory analysis alone. Using an idealized tracer, Pierrehumbert and Yang (1993) demonstrated the efficiency of isentropic mixing between high latitudes and the tropics. In this study, we will quantify the influence of isentropic mixing and transport from the stratosphere into the tropical midtroposphere using a Lagrangian transport model with an artificial stratospheric tracer, described in section 3. The stratospheric influence in the observed HOLW air masses is subsequently identified by combining 3-D back trajectories, initialized from the locations and times of the observations during the CONTRAST, and the CLaMS stratospheric tracer distributions. Although not the main focus of this study, we also discuss the possible transport pathway for midlatitude UT influence (section 4) and the BB signatures among the observed HOLW air masses (section 5).

2. Advective Histories of the Primary and Secondary Mode Based on 3-D Back Trajectories

As the first step of our analysis, we examine the advective footprints of the observed primary and secondary modes using 20-day 3-D back trajectories from the space-time locations of 60-s averaged in situ data from National Center for Atmospheric Research (NCAR) research aircraft Gulfstream V (GV). In total, 646 trajectories are initialized along the CONTRAST research flight tracks within the potential temperature range between 320 and 340 K (~ 4–8 km) where the HOLW anticorrelations frequently occurred (Pan et al., 2015). To focus on the TWP regional observations, three transition flights (RF01, RF02, and RF16) are excluded (for more details

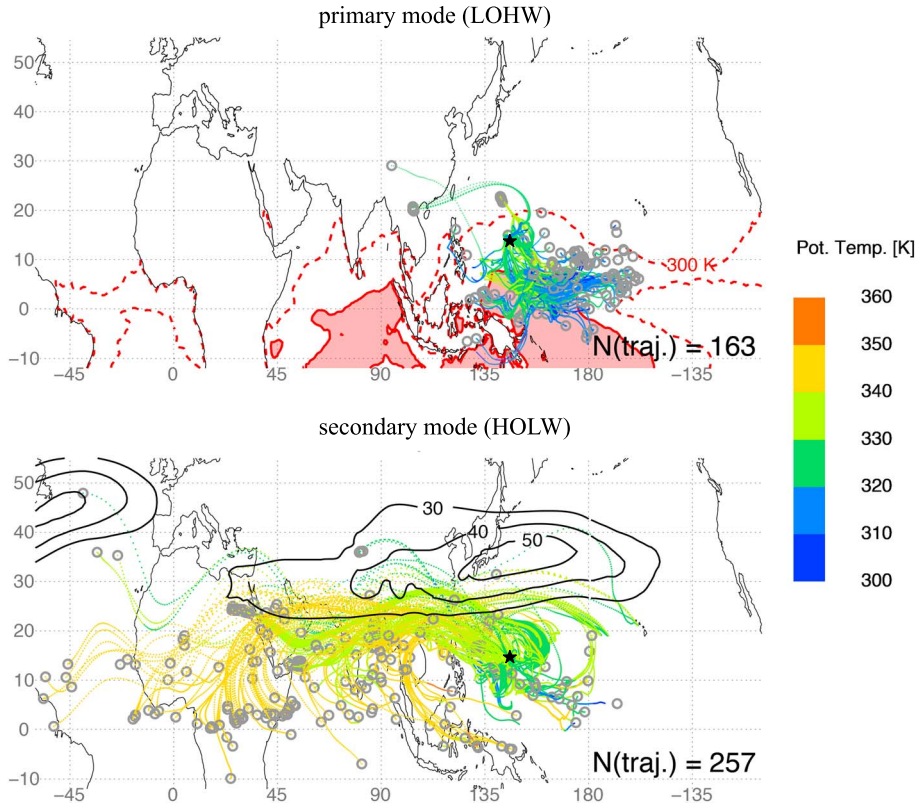

Figure 1. In total, 646 back trajectories are started from the 60-s averaged CONTRAST data between 320 and 340 K. Top and bottom panels show the 163/257 7-day back trajectories initiated from the primary (LOHW) and secondary mode (HOLW), respectively. Trajectories are color coded with potential temperature marked hourly along the trajectories. Gray circles denote the locations (footprints) where back trajectories originated 7 days earlier. The red contours in the top panel show the mean sea surface temperature (SST > 300 K) during JF 2014 and the region with SST ≥ 302 K is filled with red. The black contours in the bottom panel denote the mean zonal wind on the 320-K isentrope during JF 2014. The black star marks the location of Guam. CONTRAST = Convective Transport of Active Species in the Tropics; LOHW = low ozone and high water vapor; HOLW = high ozone and low water vapor.

of the CONTRAST research flights, see Pan et al., 2017). The calculations used the trajectory module of the Chemical Lagrangian Model of the Stratosphere (CLaMS) driven by (ECMWF) ERA-Interim horizontal winds and diabatic heating rates (Dee et al., 2011; Ploeger et al., 2010).

Following the procedure described in Pan et al. (2015) and Anderson et al. (2016), the observed anticorrelated H_2O and O_3 mixing ratios are used to identify the primary (LOHW) and secondary (HOLW) mode. Thus, the air parcels with O_3 < 30 ppbv and simultaneously observed RH > 45% are defined as the primary mode (Pan et al., 2015), while those with O_3 > 40 ppbv and RH < 20% are defined as the secondary mode. The primary mode shows a very narrow distribution of O_3 with mixing ratios 18 ± 5 ppbv. The criteria for the secondary mode in our study are the same as the criteria used in Anderson et al. (2016) defined for HOLW: O_3 > 40 ppbv and simultaneously RH < 20%. Randel et al. (2016) also used RH < 20% to define the dry layers.

Among the 646 trajectories, there are 163 and 257 trajectories representing the primary and the secondary mode, respectively. Figure 1 shows the hourly *footprint* of 7-day back trajectories of the air parcels in both primary and secondary modes, respectively, color coded by the air parcels' potential temperature. Note that only the last 7-day trajectories before the observations are shown in Figure 1 because the 7-day time window is enough to diagnose the different origins associated with two modes. The results show that the trajectories from the primary mode mostly trace back to the western Pacific warm pool on the eastern side of Guam where the high sea surface temperature (SST ≥ 302 K region shown by the red shading) and low outgoing long-wave radiation (OLR, not shown) were located during the CONTRAST period. Most of these primary mode air parcels ascended over the western Pacific before being observed, consistent with findings discussed in Pan et al. (2015) and Anderson et al. (2016).

The 1-week back trajectory footprints of the secondary mode air parcels exhibit a very different history. Most air parcels came from the far western side of Guam and were advected eastward along the equatorward flank of the subtropical jet. Toward the end of the journey, these air parcels followed the anticyclonic flow and descended into the midtropospheric TWP. The footprints indicate that the air parcels were mainly in the tropical upper troposphere and partially in the NH subtropics 7 days before the observation (the gray circles in Figure 1). Extended back trajectories, up to 10 days, indicate cross-equator transport over the Indian Ocean as well as long-distance transport from the west across the tropical Atlantic Ocean (not shown).

Overall, our trajectory study demonstrates the distinct transport pathways for the primary and the secondary modes, supporting the hypothesis of Pan et al. (2015) on the TWP convective-controlled primary mode and the nonlocal large-scale transport-controlled secondary mode. The Lagrangian foot prints show that transport is largely within the tropics and associated with the descending branch of the Hadley cell, consistent with the result discussed in Anderson et al. (2016).

Although the pure trajectory approach is a convenient and widely used tool for diagnosing the (advective) history of air, this approach completely neglects the mixing process between air parcels transported along the trajectory and surrounding ambient air. This error increases significantly with the increasing length of the trajectory, especially near the subtropical jet where RWB may dominate the flow (Postel & Hitchman, 1999; Waugh & Polvani, 2000) and where bifurcation points can be found (i.e., trajectories launched in the vicinity of such point behave nonlinearly in the sense that a small change of their initial positions causes a sudden *qualitative* change in their long-term behavior; Bowman et al., 2007; Scott & Cammas, 2002).

3. Model Simulations and Analyses of Transport

To include mixing into trajectory studies either diffusive reconstruction (Legras et al., 2005; Stohl et al., 2005) or flow deformation-driven mixing can be used. In this study we use Chemical Lagrangian Model of the Stratosphere (CLaMS) where mixing is parameterized based on flow deformation (CLaMS mixing parameterization is discussed in section 3, and for more details, see McKenna et al., 2002 and Konopka et al., 2004). A number of STE studies using the CLaMS model have demonstrated that the observed mixing layer between the stratosphere and the troposphere is well represented in the model (Vogel et al., 2011) and that this layer itself is mainly formed by (isentropic) eddy mixing on synoptic-to-seasonal time scales (Konopka & Pan, 2012; Pan et al., 2006). Following the approach described in Konopka and Pan (2012), we use a combination of the 2-D CLaMS isentropic simulation (CLaMS-2D) and 3-D trajectory analyses to investigate the contribution of isentropic transport processes (i.e., advection plus mixing), which may explain stratospheric contributions to the observed high ozone in the TWP. In the next section, we show the dominant role of such isentropic transport by comparing CLaMS-2D both with a full 3-D Chemistry Climate model (CCM) run as well as with the observations.

3.1. CLaMS Model Simulation of Isentropic Mixing

To quantitatively estimate the contribution of STE to the tropical troposphere via isentropic mixing, an isentropic run of CLaMS (CLaMS-2D) is performed. Hereby, simulations of an idealized stratospheric tracer (T_{str}) were performed using 10 quasi-isentropic layers defined by the hybrid coordinate (ζ) with ζ following the dry potential temperature θ between 300 and 390 K (every 10 K) roughly above $p_r = 700$ hPa (for more details see Appendix A). The mean horizontal distance between the initialization points of the Lagrangian air parcels is approximately 100 km. Trajectories driven by ERA-Interim wind along isentropic layers determine the position of air parcels. Deformations due to the wind shear are quantified by the Lyapunov exponent λ. After each 6-hr trajectory, CLaMS allows the air parcels to mix on each isentropic surface where the deformations are sufficiently strong, that is, the Lyapunov exponent λ is larger than a critical value λ_c (choice of λ_c for run in 6-hr time step, see Vogel et al., 2011) The mixing of parcels results in a change of their chemical composition. (for more details, see McKenna et al., 2002 and Konopka & Pan, 2012).

The CLaMS run covers the period from October 2013 to December 2014. At the beginning of the simulations, the stratospheric tracer T_{str} is initiated to a constant value of 1 in the stratosphere and to 0 in the troposphere using the 3 PVU isopleth as the mean dynamical tropopause (Kunz et al., 2011). To mimic tropospheric ozonem which has an averaged tropospheric lifetime of about 23 days (Stevenson et al., 2006; Young et al., 2013), T_{str} undergoes exponential decay with a 20-day lifetime ($\tau = 20$ days) everywhere in the troposphere. After 3 months of the simulation, the zonal mean distribution of T_{str} reaches a quasi-steady state. In Appendix B, we

discuss the sensitivity of our result to different choices of the *e*-folding constant (τ = 10 days or 30 days) and compare the lifetimes of our tracer with modeled ozone lifetimes.

3.2. CLaMS-2D Versus CAM-Chem and Observations

As described above, CLaMS-2D simulations extract the isentropic (i.e., adiabatic) processes from the full transport. Thus, diabatic processes, for example, the large-scale ascent, descent, convection, and its related vertical mixing, are neglected in such a simulation. To characterize the importance of isentropic processes simulated with CLaMS-2D, we need a referential simulation that performs full transport with more comprehensive chemistry. In this section, we describe the comparison with such a referential simulation using a 3-D CCM, CAM-chem. The specific goals of the comparisons are threefold: (1) to demonstrate that the isentropic transport is the dominant process for stratospheric influence in the tropical midtroposphere, (2) to support the design of the idealized stratospheric tracer T_{str} in CLaMS simulation, and (3) to provide a basis for estimating the minimum value of T_{str} to be considered significant stratospheric influence.

The Community Atmospheric Model with chemistry, version 4 (CAM-chem) is a part of the Community Earth System Model version 1 (CESM1), a coupled CCM from the surface to the upper stratosphere (Lamarque et al., 2012). In this study, a *specified dynamics* version of CAM-chem is used, where the (external) meteorological fields (Lamarque et al., 2012) come from the NASA Global Modeling and Assimilation Office (GMAO) Goddard Earth Observing System Model, Version 5 (GEOS5; Rienecker et al., 2008). Here temperature, zonal and meridional winds, and surface pressure are nudged with a 5-hr relaxation time constant to drive the physical parameterization that control boundary layer exchanges, advective and convective transport, and the hydrological cycle. In this work, CAM-chem contains 56 vertical levels from the surface to 1.86 hPa. The vertical coordinate is purely isobaric above 100 mb, but is hybrid below that level. The vertical resolution is variable: ~1.6 km near the stratopause, ~1.2 km in the lower stratosphere, and ~1.1 km in the troposphere (except near the ground where much higher vertical resolution is used in the planetary boundary layer). The horizontal resolution is 0.95° × 1.25° (latitude × longitude). The model includes a comprehensive chemistry scheme to simulate the evolution of trace gases and aerosols in the troposphere and the stratosphere (Fernandez et al., 2014; Kinnison et al., 2007; Lamarque et al., 2012; Ordóñez et al., 2012; Saiz-Lopez et al., 2014). This version of CAM-chem was used during CONTRAST (Pan et al., 2017), and the model setup is consistent with the Chemistry Climate Model Initiative (CCMI) REF-C1SD experiment (Tilmes et al., 2016).

In this study, we use the mixing ratio of the *stratospheric*O_3 tracer (O_3S) from the CAM-chem simulation, which is designed to represent the amount of O_3 photochemically produced in the stratosphere, transported and destroyed in the troposphere. This tracer has been used in a series of model studies (e.g., Emmons et al., 2003; Roelofs & Lelieveld, 1997; Wang et al., 1998). The CAM-chem O_3S field is produced by setting $O_3S = O_3$ above the lapse rate based tropopause. Below the tropopause, the ozone loss processes for the full chemistry solution is applied to the O_3S tracer. O_3S is also dry deposited on the surface in the same manner as the solution O_3.

Conceptually, both O_3S and T_{str} quantify the stratospheric influence in the troposphere. On the other hand, O_3S from CAM-chem represents the stratospheric ozone from full transport processes with a comprehensive chemical evolution, whereas T_{str} is a process diagnostic tracer representing only isentropic processes with a simplified exponential decaying. Thus, when comparing the O_3S and T_{str} fields with the two model simulations, we do not expect the two fields to have identical structure. Instead, we expect two fields to show a large degree of similarity if the CLaMS-2D isentropic simulation represents the dominant transport process for significant amount of stratospheric O_3 in the tropical midtroposphere.

The CLaMS T_{str} and CAM-chem O_3S distributions on the 320-K isentrope and the vertical cross section along the 137.5°E for three selected days are shown in Figures 2 and 3, respectively. This sequence of days provides an example for mixing of midlatitude LS air into the tropics, a process frequently observed during the CONTRAST period and clearly represented by both model runs. In Figure 2, equatorward RWB results in the southwestward transport of stratospheric air toward the tropics shown on 24 January. In the following two days, the high values of T_{str} moved eastward with the westerlies and arrived in Guam on 26 January. The values of both T_{str} and O_3S are largely diluted in the deep tropics, but filaments of air with $T_{str} \geq 15\%$ and $O_3S \geq 10$ ppbv are widely spread over the TWP from both models. These largely diluted but still pronounced stratospheric influences represented by T_{str} are a result of irreversible isentropic mixing, which cannot be reproduced through the back trajectories discussed in the previous section.

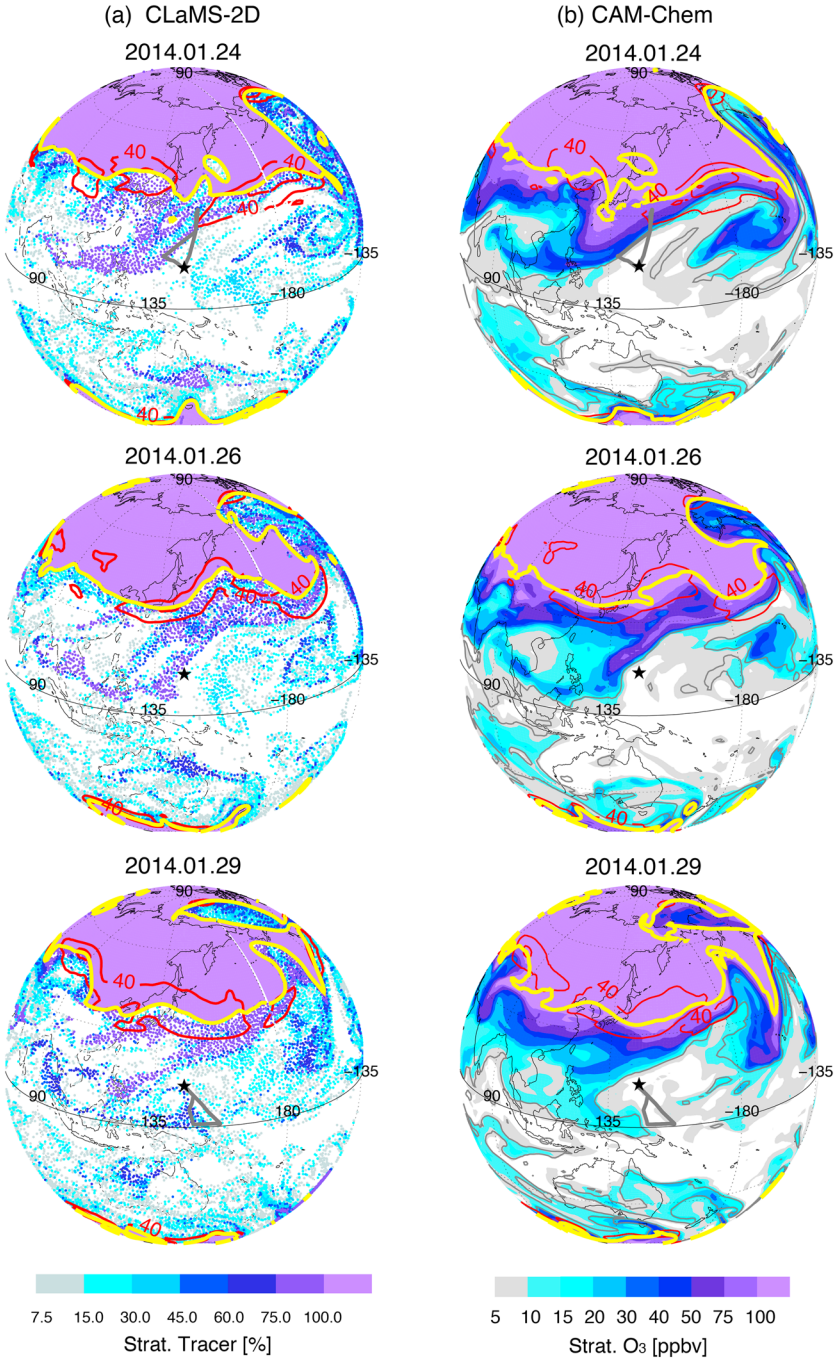

Figure 2. Stratospheric tracer with CLaMS-2D (left panel, T_{str} in unit of %) and stratospheric O_3 with CAM-chem (right panel, O_3S in unit of ppbv) on 24, 26, and 29 January on the 320-K isentrope. The gray contours in the right panel show 40 ppbv isolines of the total ozone. The solid yellow contours denote the 3 PVU isoline. The red contours show the zonal wind larger than 40 m/s with 20 m/s interval. The black star marks the location of Guam. The flight tracks of RF06 (on 24) and RF07 (on 29) are shown as the thick gray lines. CLaMS-2D = Two-Dimensional Chemical Lagrangian Model of the Stratosphere; CAM-chem = Community Atmospheric Model with chemistry, version 4.

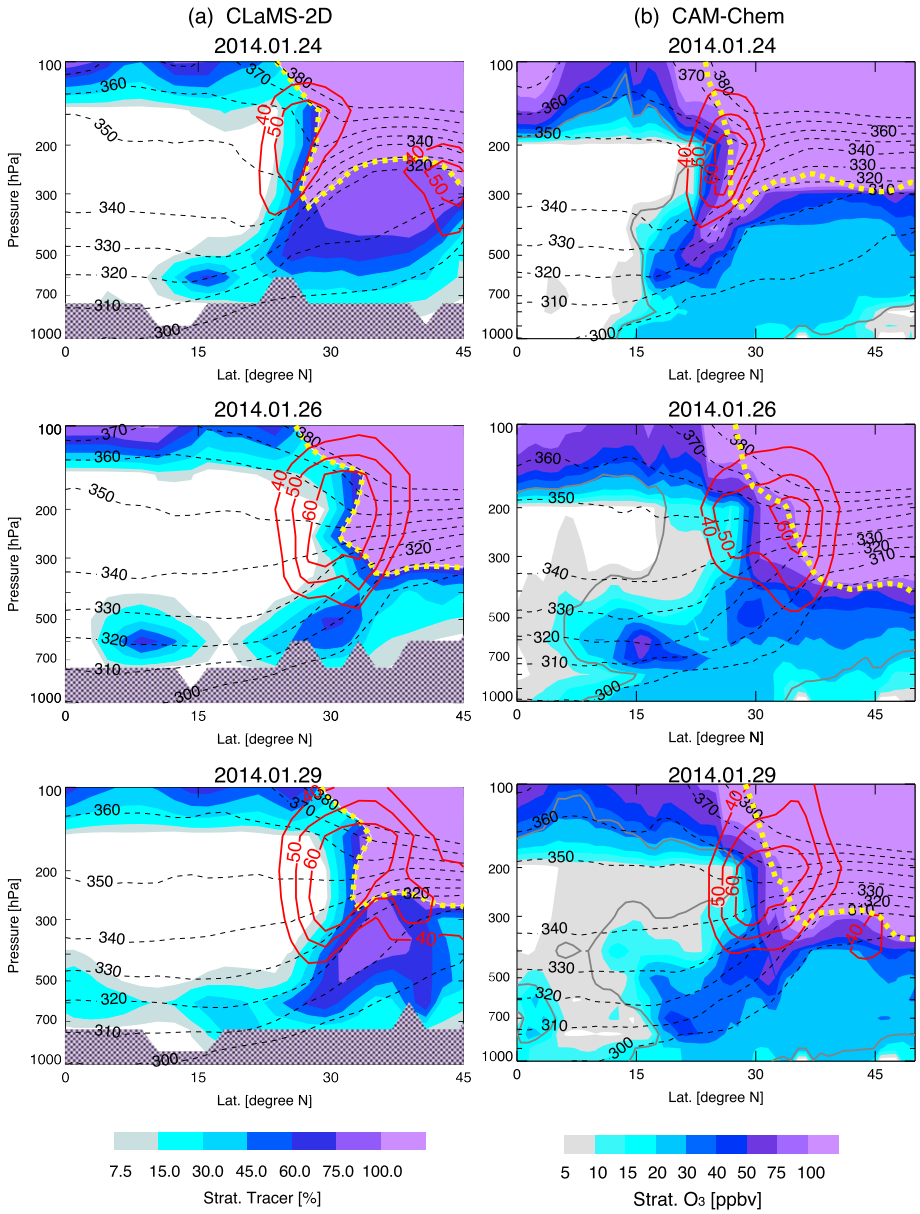

Figure 3. Cross section along 137.5°E of T_{str} and O_3S shown in Figure 2 on 24, 26, and 29 January. Similar as in Figure 2, the gray lines show the 40 ppbv isolines of total ozone, the yellow contours denote the 3 PVU isolines, and the red contours quantify the zonal wind larger than 40 m/s with 10 m/s interval. The region where missing values exist (close to lower boundary of the model) is covered by the dark gray shade. CLaMS-2D = Two-Dimensional Chemical Lagrangian Model of the Stratosphere; CAM-chem = Community Atmospheric Model with chemistry, version 4.

In Figure 2, we show filamentary structures with enhanced T_{str} values up to 60% in the tropics. Most of these filamentary structures are also captured by O_3S from CAM-chem but are not as pronounced as in CLaMS. This difference in part reflects the difference in the two models' gridding methods. The CLaMS is an adaptive grid model, where an explicit flow deformation-driven mixing parameterization is used to control the numerical diffusivity. This method allows CLaMS to represent the strong inhomogeneity of mixing and preserves the filamentary structure created by stirring and stretching (Konopka et al., 2004; McKenna et al., 2002; Pan et al., 2006). On the other hand, CAM-chem, like in all regular-grid Eulerian models, contains intrinsic diffusivity which reduces the tracer gradients within small structures like filaments (Hoppe et al., 2014; Khosrawi et al., 2005). Additionally, the lack of explicit convective transport in CLaMS-2D will likely result in an underrepresentation of strong sink of O_3 over the oceanic lower boundary. Consequently, T_{str} from CLaMS-2D tends to overestimate the stratospheric influence over the region controlled by oceanic convection.

Note that the wind fields and the isentrope structures from the CLaMS-2D and CAM-chem runs are not identical, as shown in Figures 2 and 3. These differences reflect the differences between the two dynamical fields, GEOS5 and ERA-Interim. We do not expect these differences to influence the general behavior of the RWB-driven transport process that we aim to characterize. To demonstrate this, we have included a 10-day animation as supporting information S1, which shows that the 10-day space-time evolution of the two tracers are highly consistent, despite the differences in wind field details.

Despite the differences in details, the qualitative agreement between the CLaMS T_{str} and CAM-chem O_3S supports our argument that the isentropic transport process represented by CLaMS-2D is the dominant process for bringing stratospheric influence to the tropics. Specifically, the vertical cross sections (Figure 3) show that both stratospheric tracers are largely confined to the 310- to 330-K range, a layer beneath the jet core. This behavior is consistent with previous studies that identified the contribution of midlatitude UTLS air to *dry intrusions* (Cau et al., 2005; Randel et al., 2016; Yoneyama & Parsons, 1999) and to high ozone in the tropical troposphere (Hayashi et al., 2008; Pan et al., 2017). It is also seen in Figure 3 that T_{str} from CLaMS shows weaker stratospheric influence in the layer $\theta = 330–340$ K compared to CAM-chem. This difference could relate to the weak penetration of T_{str} across the jet core compared to O_3S from CAM-chem. The mixing across the jet core in the atmosphere is associated with all types of jet stream instabilities typically driven by the flow deformations and vertical temperature gradients. These processes are represented, at least to some extent, by the CLaMS mixing parameterization driven by the large-scale ERA-interim meteorology but can be overestimated by the ubiquitous numerical diffusivity of the Eulerian models.

Finally, Figure 4 compares the simulated T_{str} (red, right panels) with the observed O_3 (black, left panels) for the research flights RF06 and RF07 (see the flight tracks of RF06 and RF07 shown as the thick gray lines in Figure 2). Note that this comparison is qualitative and aims to identify whether the modeled T_{str} is consistent with the observed O_3 elevated layer. In both cases, elevated T_{str} are found to colocate with the observed O_3 enhancement. In the case of RF07, the modeled and observed layers are well colocated in the vertical structure. In the case of RF06, the observed O_3 enhancement has a broad layer in the 3- to 9-km altitude layer, but the modeled T_{str} is approximately half of the vertical range between (~3–6 km, top panel of Figure 4). The 3-D trajectory calculations performed for this flight (RF06) show that the secondary mode air masses observed in the layer between 6 and 9 km trace back to the upper troposphere near the subtropical jet, where O_3 has typical mixing ratio of 60 ppbv or greater. This missing representation in the upper part of the elevated O_3 structure reflects the possibility that air masses from the midlatitude upper troposphere also contribute to the observed ozone enhancement via diabatic process.

The similar behavior between the T_{str} from CLaMS-2D and O_3S from the CAM-chem model as well as between T_{str} and the observed ozone enhancement in the layers $\theta = 310–330$ K, supports our contention that T_{str} represents the stratospheric influence well on the tropical ozone in the 310- to 330-K layers. The consistency between the CLaMS T_{str}, CAM-chem O_3S and the observed O_3 supports the significant role of isentropic transport from the LS into the tropical troposphere. The contribution of this process to the formation of the observed HOLW air masses is further analyzed in the next section. On the other hand, the insufficient representation by T_{str} for observed O_3 enhancements in the higher layers ($\theta = 330–350$ K) suggests that diabatic processes and the midlatitude UT contributes to these layers.

4. Stratospheric Contributions to the HOLW Observations Via Isentropic Mixing

The CLaMS model result discussed in the previous section demonstrated pervasive stratospheric influence in the tropical troposphere through isentropic mixing. As an irreversible part of the adiabatic transport process, this mixing process is not represented in the trajectory calculations as shown in section 2. This finding suggests that, although the Lagrangian footprints of the secondary mode air masses are largely equatorward of the subtropical jet with no direct indication of STE histories, their transport pathways may have encountered mixed air masses containing a pronounced stratospheric fraction. Therefore, it is necessary to reexamine the 3-D back trajectories of secondary mode air masses through evaluating the significance of stratospheric influence along these trajectories.

As a process study, the goal of the following diagnosis is not to quantify how much stratospheric O_3 is in the secondary mode layer but rather to quantify how often the stratospheric influence made a significant contribution to the observed secondary mode layer through 3-D advection in conjunction with isentropic mixing. Therefore, results shown in Figures 2–4 justify T_{str} as a diagnostic quantity of STE via isentropic process.

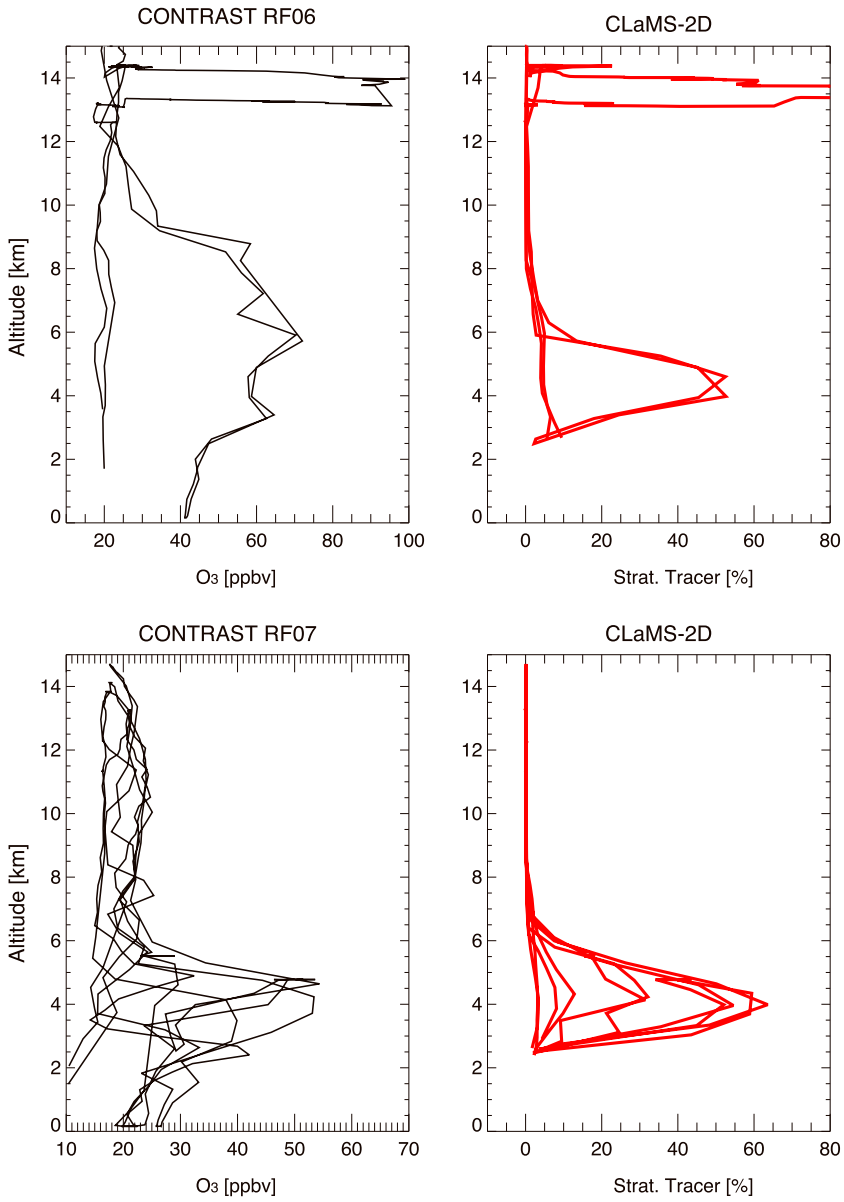

Figure 4. O_3 profiles observed during 24 January (RF06) and 29 January (RF07) and the corresponding stratospheric tracer with 20-day tropospheric lifetime from CLaMS-2D run interpolated along the flight tracks shown as the thick gray lines in Figure 2. CLaMS-2D = Two-Dimensional Chemical Lagrangian Model of the Stratosphere; CONTRAST = Convective Transport of Active Species in the Tropics.

In the following section 4.1, we are going to determine a threshold of T_{str}, which quantifies the significance of stratospheric influence.

4.1. Threshold for Significance of Stratospheric Contributions

To diagnose the stratospheric contribution to observed HOLW layer, we need an estimate of a threshold value of T_{str}, above which the stratospheric influence will add enough ozone for the air mass to be classified as the HOLW mode. This threshold value is derived combining the O_3 information from CAM-chem simulation and some approximations of the transport pathways, which are described below.

As a simple approximation, tropical midtroposphere air can be considered as a mixture of mass fractions from the convective oceanic air (F_{conv}) and from the midlatitude UTLS. The midlatitude UTLS fractions can be further divided into fractions of the midlatitude upper troposphere (F_{UT}) and the midlatitude lower stratosphere (F_{LS}),

that is,

$$F_{conv} + F_{LS} + F_{UT} = 1. \quad (1)$$

Because this study is designed to focus on the stratospheric contribution, the T_{str} threshold value of interest is under the condition of $F_{UT} = 0$, that is, those HOLW air masses formed by only adding stratospheric in-mixing to the background air mass of convective origin. The choice of $F_{UT} = 0$ here, therefore, does not imply the UT influence to be unimportant or negligible. As we show later, the result of this simplification in effect is to separate the HOLW air masses formed from stratospheric in-mixing from those likely formed from midlatitude UT influence.

Given $F_{UT} = 0$, equation (1) reduces to

$$F_{conv} + F_{LS} = 1. \quad (2)$$

In this case, the O_3 mixing ratio in the tropical midtroposphere (O_{3tmt}) has the following relation:

$$O_{3tmt} = F_{LS} \cdot O_{3_{LS}}' + (1 - F_{LS}) \cdot O_{3_{conv}}'. \quad (3)$$

Note that the O_3' mixing ratios on the right side of this equation are not the O_3 mixing ratios in their original regions but the O_3 mixing ratios from their origins (corresponding to the subscripts) after a degree of chemical evolution associated with the transport time from their origins to the observation location (tropical midtroposphere).

Now we include the chemical evolution of O_3 from its origin region to the observation location as a chemical evolution rate (R). In the atmosphere, R is a complex result of transport time and O_3 chemical loss rate associated with specific background conditions, for example, UV radiation and NO_x background. For the transport process from the midlatitude lower stratosphere, the chemical evolution rates refer to R_{LS}, that is,

$$O_{3_{LS}}' = R_{LS} \cdot O_{3_{LS}}, \quad (4)$$

where $O_{3_{LS}}$ is O_3 mixing ratio in the midlatitude lower stratosphere where and when STE occurred. Note that the chemical evolution of O_3 from convective uplifting is not discussed because $O_{3_{conv}}'$ can be estimated by the observations of primary mode ozone, that is, $O_{3_{conv}}$ ~20 ppbv.

Replacing $O_{3_{LS}}'$ by equation (4), a further relationship among the quantities in equation (3) is given by

$$O_{3tmt} = F_{LS} \cdot R_{LS} \cdot O_{3_{LS}} + (1 - F_{LS}) \cdot O_{3_{conv}}'. \quad (5)$$

Besides $O_{3_{conv}}'$ ~20 ppbv, other quantities in equation (5) can also be obtained from observations and the model. The $O_{3_{LS}}$ can be estimated by O_3 averaged along the 3 PVU isopleth within the isentrope 320–340 K from the CAM-chem model (see section 3.2), which has typical values ~150–250 ppbv. Consistent with the design of T_{str} in the CLaMS simulation, the chemical evolution rate R_{LS} can be simplified as the 20-day exponential decay; that is,

$$R_{LS} \approx e^{-t/\tau}, \quad (6)$$

where $\tau = 20$ days and t is the decay time for an individual air mass. With the decay time (t) varying from 1 day to 7 days for representative transport times, which will be used in the later diagnostic study, the corresponding R_{LS} can be estimated within a range from 0.95 to 0.7.

Using these approximations of R, $O_{3_{TP}}$, and $O_{3_{conv}}$, the range of T_{str} to form the lower limit $O_{3tmt} = 40$ ppbv can be derived: T_{str} ~10% to 17%. The range of T_{str} corresponding to $O_{3tmt} = 70$ ppbv is T_{str} ~25% to 35%. This is an estimation of T_{str} for creating the elevated O_3 layer from a conceptual point of view, which neglects the complicated interaction between mixing and chemistry. In reality, one observed air mass contains the

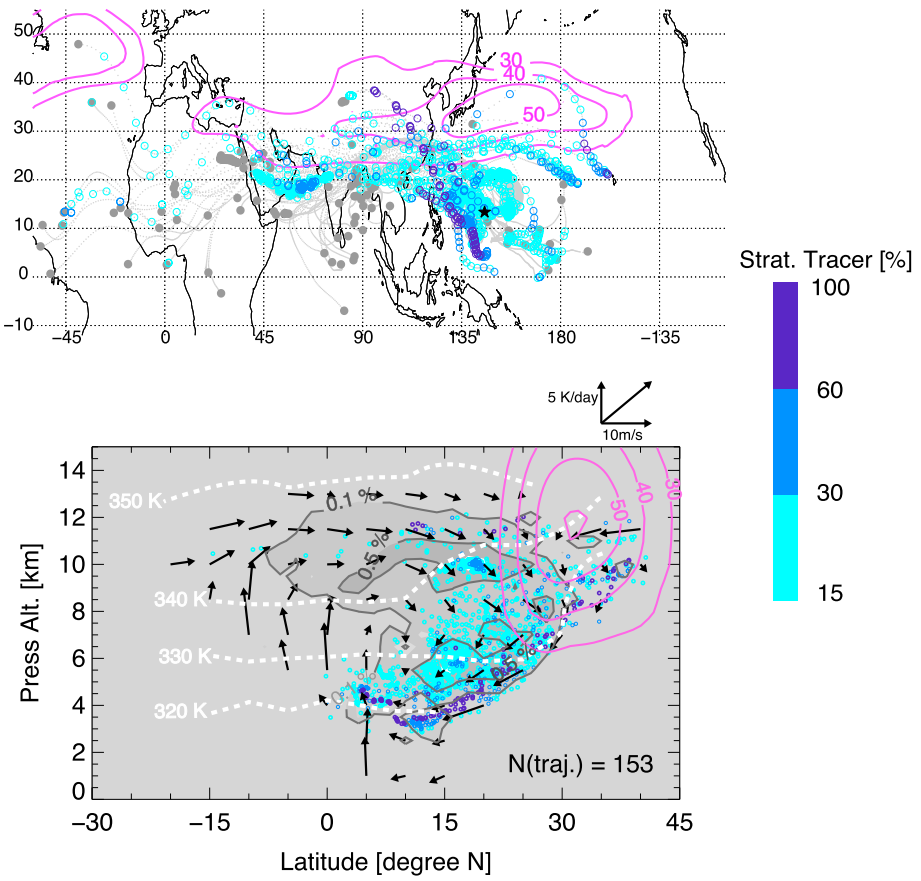

Figure 5. Subset of the secondary mode (HOLW) 7-day back trajectories with significant stratospheric influence (153 from 257, G1). (top panel) The colored circles show the stratospheric tracer ($T_{str} \geq 15\%$) marked 6-hourly along the trajectories and the purple contours show mean westerlies on the potential temperature level $\theta = 320$ K over the corresponding dates during the CONTRAST period. The bottom panel illustrates the same distribution but in the latitude-altitude space: The gray shades show the probability distribution function of the hourly footprints of 20-day back trajectories; the arrows and the purple contours respectively, show the averaged meridional and cross-isentropic velocity and the subtropical jet ($\bar{u} > 30$ m/s) averaged over the corresponding observation dates; the colored dots show the T_{str} distribution in the same color code as the circles in the top panel. HOLW = high ozone and low water vapor; CONTRAST = Convective Transport of Active Species in the Tropics.

fractions with a spectrum of transport times. In the following study, we use $T_{str} \geq 15\%$ as a reasonable estimate for the significance of the stratospheric contribution.

Further supportive information was shown in section 3.2 that the 40 ppbv total O_3 from CAM-chem (shown as the gray isoline in Figures 2 and 3) agrees well with $T_{str} \geq 15\%$ (the lightest blue color). This fact further supports that $T_{str} \geq 15\%$ is an appropriate threshold to form the lower limit of secondary mode ozone from the perspective of the models.

4.2. Connecting Significant Stratospheric Contributions to the HOLW Observations

Based on the threshold of significant stratospheric influence, we can diagnose how often the observed secondary mode air masses experienced significant stratospheric influence. The 3-D back trajectories are used to connect the modeled stratospheric tracer to observations. The stratospheric tracer T_{str} from the isentropic simulation is interpolated along the trajectories every 6 hr. When T_{str} along a trajectory is found to be larger than 15%, the air mass is considered to have experienced significant stratospheric influence. Otherwise, the stratospheric influence on the air parcel is considered to be insignificant.

In total, 35% of the secondary mode observations are found to have a significant stratospheric influence during 1-day back trajectories. Counting up to 7-day back trajectories, the percentage increases to 60%. However, the stratospheric influence barely increases for longer than 7-day back trajectories: additional 10% (total of 70%) are found using the 15-day back trajectories. Considering the relatively short lifetime of stratospheric

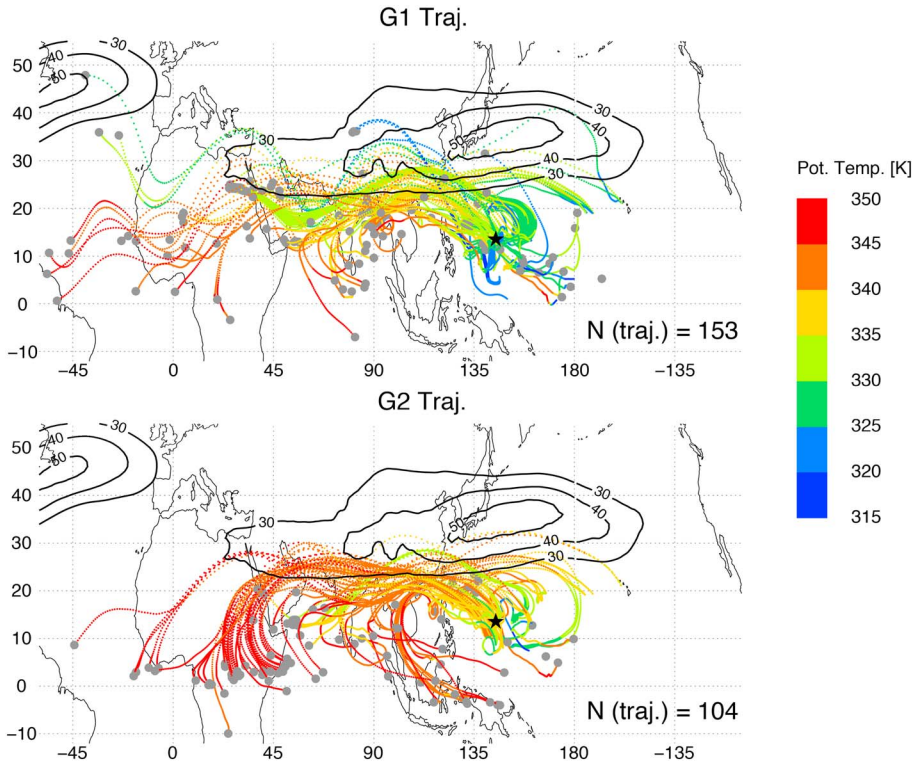

Figure 6. The two groups of back trajectories related to the secondary mode (HOLW) shown in Figure 1: G1 trajectories with significant stratospheric influence (top) and G2 trajectories with insignificant stratospheric influence (bottom). The colors show the potential temperature marked hourly along the trajectories, and gray circles show the locations where trajectories end. The black contours show the westerlies averaged over the corresponding observation dates of each group. The black star marks the location of Guam. HOLW = high ozone and low water vapor.

ozone once arriving in the tropics, only encounters which occurred within 7 days before the observations are counted for our analysis (*fresh* in-mixing).

Figure 5 depicts the locations along the back trajectories where significant stratospheric influences are encountered, that is, 6-hourly T_{str} values larger than 15% along the trajectories (color-coded circles). It can be seen that the stratospheric influences are encountered for a wide latitudinal and longitudinal range, from near the equator to the core of the subtropical jet. In the vertical cross section, the significant influence is mostly below the level of the jet core (320–340 K). The background flow experienced by the air parcels is also displayed in Figure 5: the end points of 7-day back trajectories are shown as small gray dots in the top panel and the probability distribution function (PDF) of the hourly footprints for the 20-day back trajectories are shown as the gray shades in the bottom panel. The dominant circulation pattern is consistent with the descending transport near the subtropical jet (see the arrows in the bottom panel), where most of the encounters with stratospheric influence air occur. Note that the values of the stratospheric tracer in Figure 5 is mostly between 15% and 30% while only a few trajectories show a higher stratospheric influence (~60%).

This diagnosis enables us to categorize the secondary mode air masses into two groups, G1 and G2, according to whether their back trajectories encountered significant stratospheric influences within 1 week before being observed. Among the 257 secondary mode trajectories (as shown in Figure 1), 60% (153 trajectories) experienced a significant stratospheric influence (G1) and the remaining 40% (104 trajectories) did not (G2). The plane view and the meridional cross section of trajectory histories for the two groups are shown in Figures 6 and 7 together with the derived background large-scale flow patterns. Note that the lengths of back trajectories used in Figures 6 and 7 are different. Figure 6 shows the trajectory histories 7 days before the observations. Figure 7 shows the probability distribution of the hourly footprint based on 20-day back trajectories, which completes a longer advective transport history of the air parcels.

The plane view (Figure 6) highlights the differences between G1 and G2 in their potential temperature histories. While the G1 parcel trajectory footprints within 7 days are largely below 340 K (in yellow and green),

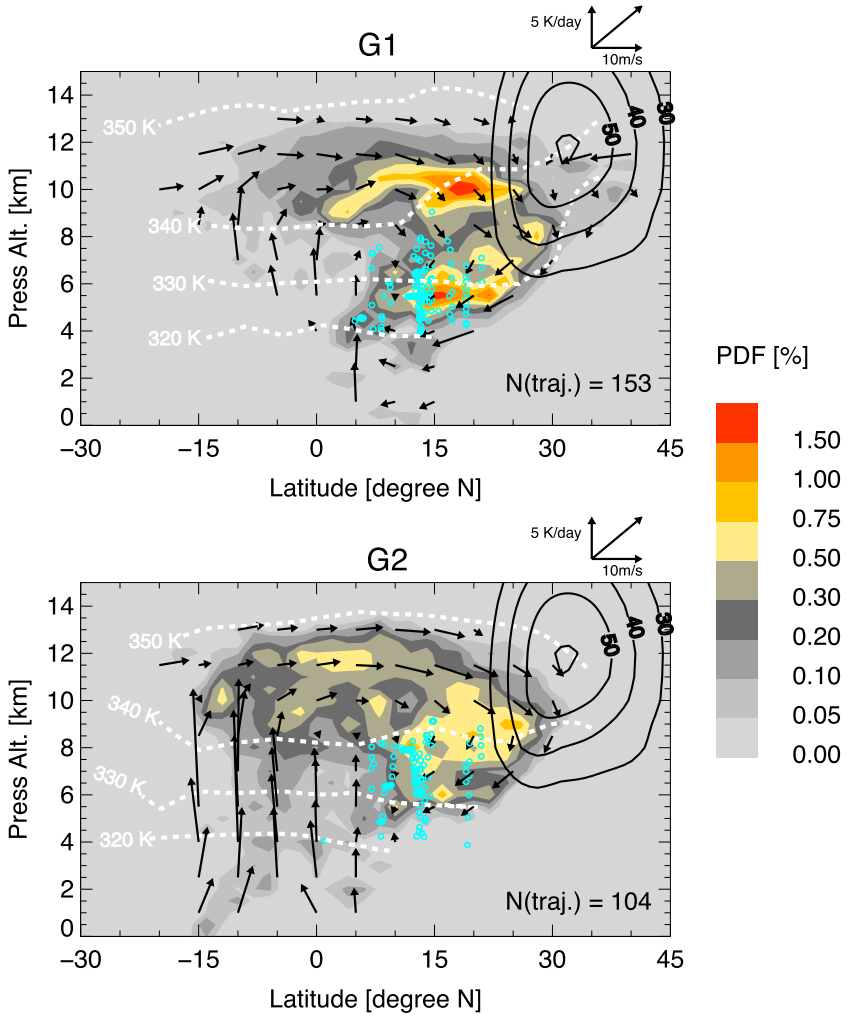

Figure 7. The frequency distribution of trajectory footprints along latitudes and pressure altitudes corresponding to the two groups in Figure 6. The hourly footprints of trajectories back to 20 days are used for the probability distribution function calculation. The black contours show the subtropical jet ($\bar{u} > 30$ m/s) averaged over the corresponding observation dates of each group. The arrows show the averaged meridional and cross-isentropic velocity along the trajectories. The white dashed lines denote the mean potential temperature. The cyan circles show the locations of the HOLW signatures from the 60-s averaged observations. HOLW = high ozone and low water vapor.

the G2 footprints are mostly above 340 K (in orange and red). Moreover, G1 parcels typically followed along the subtropical jet, in most cases for 5 days or longer, whereas G2 parcels typically followed southerly flow to travel toward the jet from the equatorial region in the last 7 days before descending anticyclonically into the TWP.

In the meridional plane (Figure 7), the PDFs of the hourly footprints of 20-day back trajectories and the average wind fields calculated for the two groups of trajectories also highlight the different flow patterns that the two groups experienced. The G1 footprints are found to be more concentrated near the subtropics, around or below the jet core, which is approximately 345 K in potential temperature. Furthermore, the average background wind shows equatorward flow around the jet core for G1, consistent with the cross-jet mixing of stratospheric air. The G2 distribution, on the other hand, is highly consistent with the tropical Hadley circulation of the season, which is dominated by the cross-equator flow in the 10- to 12-km altitudes following the ascending branch of the Hadley cell centered south of the equator.

These two different footprint distributions are consistent with the stratospheric influence identification, which indicates that the G1 group, as a *jet-following* group, is more likely influenced by in-mixing across the lower flank of jet, and the G2 group, as a Hadley circulation following group, has experienced overturning near

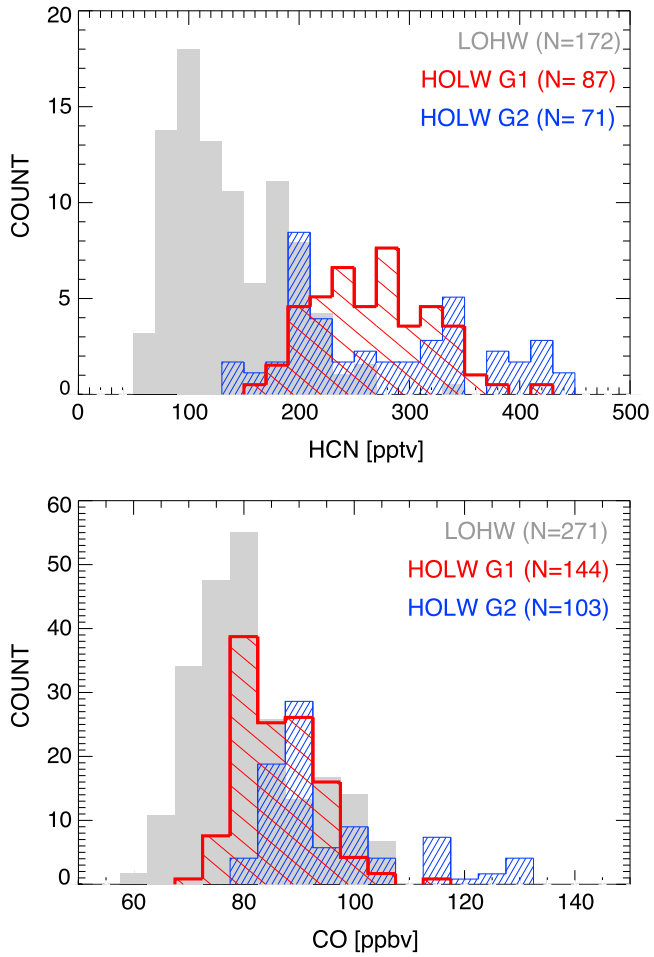

Figure 8. The distribution of HCN and CO 60-s averaged CONTRAST observations separated by LOHW (gray bars) and HOLW (red and blue bars). The HOLW observations are further categorized into significant stratospheric influence group (G1, red) and an insignificant stratospheric influence group (G2, blue). CONTRAST = Convective Transport of Active Species in the Tropics; LOHW = low ozone and high water vapor; HOLW = high ozone and low water vapor.

the equator flank of the jet before descending isentropically into the deep tropics. This process is expected to bring higher O_3 from midlatitude UT into the deep tropics (e.g., Folkins et al., 1999; Harris & Oltmans, 1997).

5. Chemical Tracer Signatures

Analyses in previous sections focused on the transport pathways experienced by the air masses in the secondary mode and the contribution by stratospheric O_3 via mixing. In this section, we examine the chemical signatures from observations and aim to identify the contribution of photochemical production of O_3 associated with BB among a number of measured chemical species we examined. HCN and CO are identified as the most effective tracers for this purpose (e.g., Palmer et al., 2013; Singh et al., 2003). Elevated CO or HCN mixing ratios over background levels are widely used to identify the BB plumes, for example, the CO mixing ratios are higher than its background +20 ppb (Alvarado et al., 2010) or CO and HCN mixing ratios are higher than its 99th percentile (mean $\pm 3\sigma$; Palmer et al., 2013). The anticorrelations between stratospheric and tropospheric tracers (in particular, O_3 against CO) were observed by in situ measurements mainly at the midlatitudes, which were widely used to identify mixing between the stratospheric and tropospheric air (e.g., Fischer et al., 2000; Hoor et al., 2002). The positive correlations among O_3, HCN, and CO in air masses influenced by BB are well-established chemical signatures, although the specific relationship between these species is dependent upon a number of factors including fire emission ratios at the source, subsequent chemical and photochemical reactions, and local and downwind meteorological patterns (Apel et al., 2015; Hornbrook et al., 2011; Jaffe & Wigder, 2012; Singh et al., 2010).

We first examine the distributions of HCN and CO using 60-s averaged observations between $\theta = 320$ K and 340 K. The HCN mixing ratios is 200 ppt with a standard deviation (σ) of 91 ppt, and for CO the mean mixing ratio with a standard deviation is 85 $\pm$ 11.5 ppbv. Their distributions, shown in Figure 8, are given in three groups, which are as follows: (1) the primary mode as identified by O_3 and H_2O, (2) G1 from mixing and Lagrangian analysis, that is, secondary mode air masses that are significantly influenced by stratospheric mixing, and (3) G2, that is, secondary mode air masses that are found not to have significant stratospheric influences.

HCN distributions show distinct features for each of the three groups. The primary mode distribution (gray bars) has low HCN (~50–200 pptv), consistent with exposure to the ocean surface, since HCN is known to have an ocean sink (Singh et al., 2003). This group shows a broad CO distribution (~60–105 ppbv), consistent with the broad spectrum of measurements, including the influence of cleaner oceanic and polluted boundary layers in the region. Distributions of both HCN and CO in G1 (red bars) are approximately Gaussian, with moderate HCN primarily between 200 and 350 pptv, and CO (~80–95 ppbv), overlapped with the primary mode distributions. These HCN and CO mixing ratios are consistent with mixed and aged midlatitude upper tropospheric air. Note that the gradient of HCN between the midlatitudes and tropics is larger than that of CO. Thus, the CO mixing ratio distribution of G1 overlaps with the primary mode, while the HCN distribution of G1 shows a higher range of mixing ratios than the primary mode.

For the distributions of G2, both CO and HCN exhibit a bimodal structure with a mode overlap with the primary mode distribution and a mode of elevated CO and HCN clearly separated from the primary mode and higher values than in the G1 group. From these distributions, we identify a group of *outliers* with CO mixing ratios greater than 105 ppbv, which is in excess of 2σ with respect to the mean value. Most of these outliers are seen from G2 with only one 60-s sample observation from G1. Similarly, the high end from HCN distribution

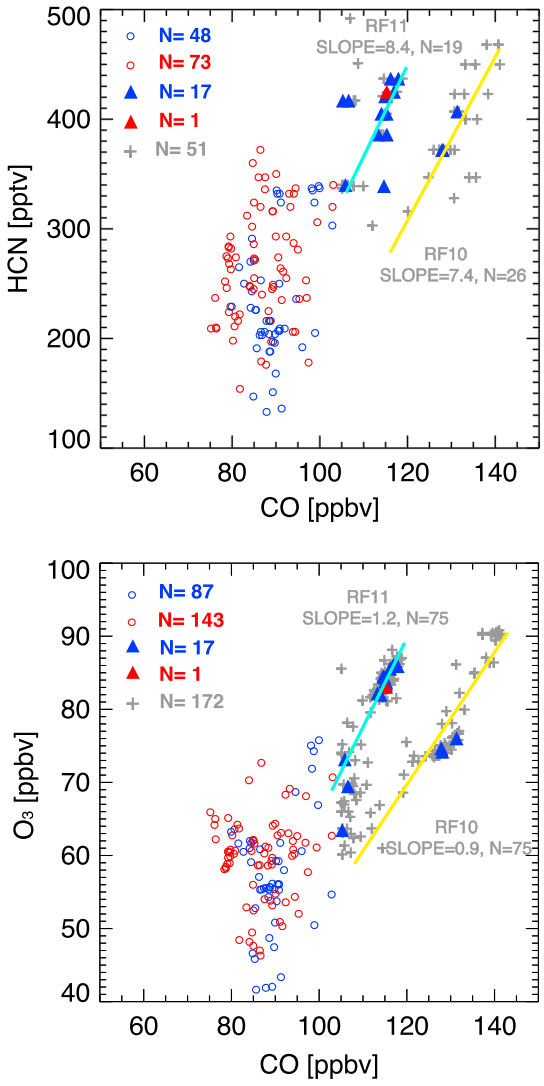

Figure 9. Scatterplots of HCN against CO (top panel) and O_3 against CO (bottom panel) 60-s averaged observations during CONTRAST for the significant stratospheric influence group (G1, red) and the insignificant stratospheric influence group (G2, blue). The circles represent observations with a CO mixing ratio < 105 ppb, and the triangles mark the observations with a CO mixing ratio ≥ 105 ppb. The 10-s averaged observations during RF10 and RF11 (gray crosses) are used to derive the linear correlations for each flight shown as the yellow and cyan lines, respectively. CONTRAST = Convective Transport of Active Species in the Tropics.

(~320 ppt) is mostly from the G2. The correlation between high HCN and CO air masses is examined in the following analyses.

Figure 9 shows scatterplots of HCN against CO and O_3 against CO for all 60-s samples in the secondary mode, color coded to identify G1 and G2 (G1 in red and G2 in blue, same as in Figure 8). In both G1 and G2, there is no clear correlation between HCN-CO and O_3-CO in the observations when CO is lower than 105 ppb (red and blue circles). Positive correlations are only present in the samples when CO is greater than 105 ppbv, identified by the triangles. These observations also correspond to elevated HCN (>320 ppt) and elevated O_3 (>60 ppb). We further analyze the chemical signatures in these observations using 10-s averaged data, shown as gray crosses in Figure 9.

About 80% of these high CO air parcels are found to be from the two research flights, RF10 (8 February) and RF11 (10 February). A linear fit for data from each of the two flights identifies strong positive correlations for both HCN-CO and O_3-CO (see blue and yellow lines in Figure 9). It has been reported that RF10 targeted a pollution plume, referred to as a *CO river* and sampled the highest mixing ratio of CO during the entire campaign (130 ppbv; Pan et al., 2017). The slope of the linear relationship ΔHCN/ΔCO (pptv/ppbv) is 7.4, and $\Delta O_3/\Delta CO$ (ppbv/ppbv) is 0.9 for RF10. These slopes are 8.4 and 1.2 for RF11.

Note that a positive quasi-linear correlation between HCN and CO as a signature of BB in the free troposphere has been observed in numerous studies of BB plumes (e.g., Alvarado et al., 2010; Apel et al., 2015; Singh et al., 2003, 2010). The enhancement ratios ΔHCN/ΔCO of BB plumes varies from 5 to 9 pptv/ppbv (Apel et al., 2015; Singh et al., 2010). The ΔHCN/ΔCO ratios are consistent with the previous studies (e.g., Apel et al., 2015; Singh et al., 2010). The $\Delta O_3/\Delta CO$ ratios are found to increase with the travel time from the fire to the observation locations (Jaffe & Wigder, 2012). Previous observations reported $\Delta O_3/\Delta CO$ from 0.2 to 0.9 ppbv/ppbv for BB plumes in tropics older than 5 days (reviewed by Jaffe & Wigder, 2012). According to our trajectory study, the secondary mode air mass are mostly older than 5–10 days. The resulting $\Delta O_3/\Delta CO$ ratios from RF10 and RF11 are consistent with longer travel times compared to these previous results.

These air masses with well-identified BB chemical signatures, given by positive HCN-CO and O_3-CO correlations, represent a small segment (~8%) of the secondary mode observations. They are mostly found in G2 (blue triangles), with only one exception (in 60-s data) from G1(red triangle). These observations are also identified in the analysis of Anderson et al. (2016), where BB is considered as the dominant source of the secondary mode.

6. Conclusions and Discussions

Motivated by the bimodal distribution of ozone in the midtroposphere (HOLW versus LOHW) observed during the CONTRAST campaign (Pan et al., 2015), we use a Lagrangian model study to diagnose the key processes that control the observed HOLW layer. This study uses a Lagrangian isentropic transport model (CLaMS-2D) and an idealized stratospheric tracer to simulate the stratospheric contribution to the tropical tropospheric ozone via isentropic transport. A 3-D Lagrangian back trajectory analysis is performed to connect the observations to stratospherically influenced air. A chemistry climate model simulation from CAM-chem, using a specified dynamics mode, is utilized to help and support the Lagrangian model diagnosis.

Qualitatively, both the CLaMS and CAM-chem show that transport from the stratosphere has a significant contribution to the chemical composition in the tropical midtroposphere. The consistency between the CLaMS stratospheric tracer and the CAM-chem stratospheric O_3 tracer supports our argument that the isentropic

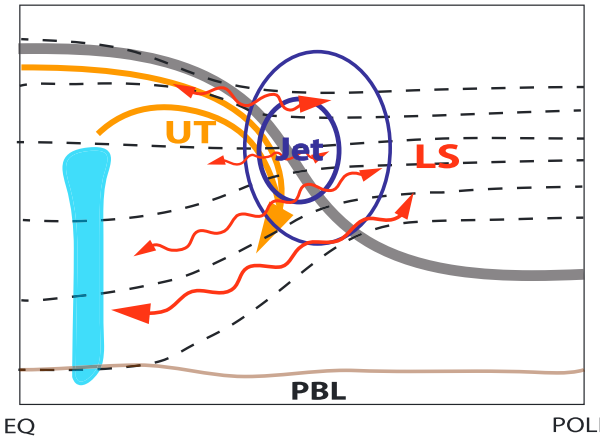

Figure 10. The key processes influencing the tropical midtroposphere: the red arrows show the transport and mixing from lower stratosphere along the isentropes; the orange thick arrow indicates the cross-equator and large-scale descending of the Hadley cell; the blue area indicates the tropical deep convection. LS = lower stratosphere; UT = universal time; PBL = planetary boundary layer.

transport is the dominant transport process between the lower stratosphere and tropical midtroposphere in the layers below the jet.

Quantitatively, we found that 60% of the observed HOLW air masses (designated as G1) contain significant stratospheric influence, while the remaining 40% (designated as G2) do not. Examination of the averaged background winds reveals that these two groups of air parcels experienced distinctly different flow patterns. The pattern for G1 parcels can be characterized as jet-following with equatorward flow below the jet core. The pattern for G2 parcels can be characterized as dominated by the cross-equator or southerly flow, followed by overturning near the equator flank of the jet, and subsequently descent into tropics. This pattern is consistent with the tropical Hadley circulation. These G2 air masses, therefore, likely contribute to the HOLW layer by bringing the midlatitude UT air during its overturning near the equator side of the jet (e.g., Folkins et al., 1999; Harris & Oltmans, 1997).

In addition to these diagnoses of transport pathways, we have also examined the chemical signature of the BB emission-facilitated ozone production, which is identified by the positive correlations among O_3, HCN, and CO. We found that approximately 8% of the observed HOLW air parcels show clear evidence of BB-facilitated O_3 production. The BB signatures are mostly identified in G2 parcels, that is, the group dominated by the Hadley circulation history. Since the BB-facilitated O_3 production and transport from the midlatitude UTLS are not a mutually exclusive process, the air masses with BB influence are likely to have photochemically enhanced ozone in addition to elevated ozone from the mixing with the UTLS air. This conclusion is consistent with the result in Figure 9 where the air parcels with identified BB signature have highest ozone.

Our results reveal that three key transport processes control the tropical midtropospheric O_3 (see conceptual diagram in Figure 10). First, convective transport of air from the oceanic boundary layer (the blue region in Figure 10) is the primary contributor to the LOHW air masses. Second, isentropic transport and mixing (the red curved arrows) efficiently brings lower stratospheric air to the tropical midtroposphere, which significantly contributes to the HOLW air masses. Third, the Hadley circulation (orange arrow) brings the upper tropospheric air to the tropical midtroposphere, which likely also contributes to the HOLW air masses.

We made two main approximations in the diagnostic study. The first approximation is represented by equation (1), where we simplified the air masses in tropical midtroposphere as coming from three *boxes* (oceanic, UT, and LS), followed by identifying the fraction of HOLW observations that contains significant stratospheric contribution (by choosing the condition of no UT contribution). Our result shows that this approximation successfully separated the LS-influenced observations from those influenced by the UT. The second approximation is to design the idealized model stratospheric tracer to have a 20-day tropospheric lifetime. By doing so, we simplify the complex O_3 chemical evolution to a constant exponential decay. This approximation likely leads to an underestimate of stratospheric contributions in the extratropics, where the O_3 lifetime is significantly longer than 20 days. Based on our further comparison (more details in Appendix B), we show that this decaying tracer is representative of the stratospheric contributions to the tropical midtroposphere.

Finally, the result of this study demonstrated the significance of representing mixing, a subgrid-scale process in modeling transport using a Lagrangian framework. Our analysis highlighted the limitation of Lagrangian back trajectory calculations, which represent only the advective transport driven by the explicit grid point winds. As demonstrated in this study, using trajectory calculation without consideration of modeling mixing may miss key physical processes that are necessary for reaching the correct interpretation of the observations.

Appendix A: Quasi-Isentropic Coordinate

An important disadvantage of potential temperature θ as the vertical coordinate is the fact that surfaces with θ = const—in particular those in the troposphere—may cross the Earth's surface. This is mainly due to latitudinal differences in the heat budget but also due to the effect of orography. To resolve transport processes

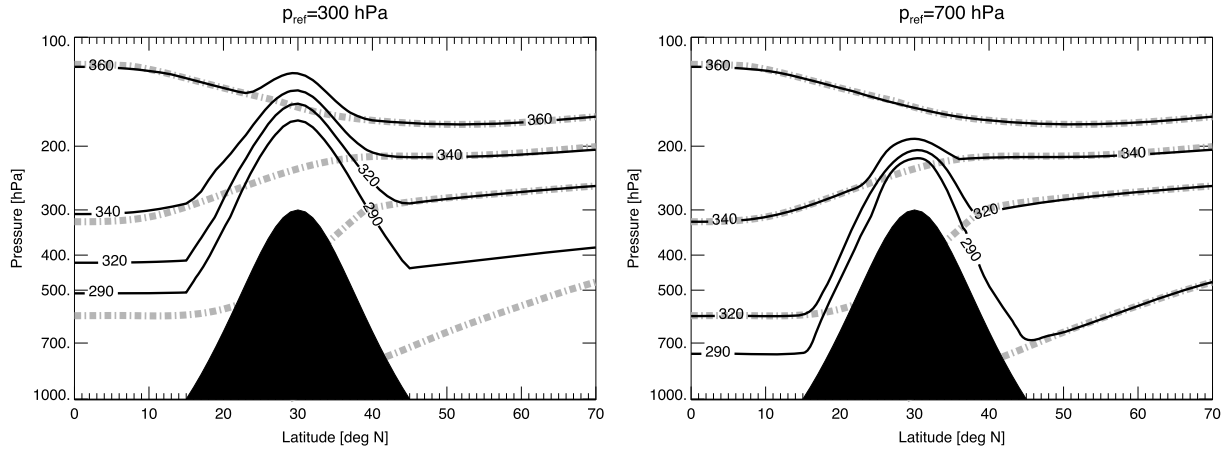

Figure A1. The ζ (thin black solid lines) and θ (thick gray dashed lines) surfaces in the pressure coordinate with reference pressure $p_r = 300$ hPa (left) and 700 hPa (right). The back region indicates an idealized orography with top pressure up to 300 hPa. To calculate these lines, equation (A1) was used as well as ERA-Interim temperature (January climatology, 1979–2013, zonal mean).

in the troposphere influenced by such effects and transport processes in the stratosphere where adiabatic horizontal transport dominates, the hybrid σ-θ coordinate ζ can be used (Mahowald et al., 2002).

More precisely, ζ is a hybrid σ-θ coordinate with σ denoting the terrain-following coordinate $\sigma = p/p_s$ (p pressure, p_s surface pressure). Following Mahowald et al. (2002), ζ is defined as follows:

$$\zeta := f(\sigma)\theta(p, T) \tag{A1}$$

with

$$f(\sigma) = \begin{cases} \sin\left(\frac{\pi}{2}\frac{1-\sigma}{1-\sigma_r}\right) & \sigma > \sigma_r \\ 1 & \sigma \le \sigma_r, \quad \sigma_r = \frac{p_r}{p_0} \end{cases} \tag{A2}$$

Here p_0 denotes the constant reference pressure level typically set to 1,000 hPa; p_r defines the pressure level around which the potential temperature θ smoothly transforms into the terrain-following coordinate σ.

For p_r Mahowald et al. (2002) used the value 300 hPa; that is, $\sigma_r = 0.3$. For situations with no orography (e.g., see surface with $p_s = p_0 = 1{,}000$ hPa) this means that the condition $\sigma = p/p_s < \sigma_r$ is valid everywhere above 300 hPa. Consequently, in this region the vertical coordinate ζ is given by the dry potential temperature θ. Conversely, below 300 hPa, θ smoothly transforms into σ. For situations with orography (e.g., at the summit of Mount Everest with $p_s \approx 300$ hPa), the condition $\sigma = p/p_s < \sigma_r$ is first valid everywhere above ≈100 hPa. Thus, above the orography the transition level above which $\zeta = \theta$ is valid shifts to higher altitudes and is given through $(p_r p_s)/p_0$.

Note that all p_r values between 0 and 1,000 hPa are possible with the consequence that higher p_r values extend the applicability of θ as a vertical coordinate down to the lower troposphere. The relation among the pressure, ζ and θ for two different choices of p_r (300 hPa, left panel; 700 hPa, right panel) is shown in Figure A1. In the orography-free region above 600 hPa, we find that θ follows the ζ surfaces by using $p_r = 700$ hPa (left panel), whereas with $p_r = 300$ hPa (right panel), this property is valid first above ~250 hPa. The ζ-coordinate for both choices of p_r transforms to terrain-following surfaces when encountering the orography. We use $p_r = 700$ hPa as the reference pressure in the study, because this coordinate allows the quasi-isentropic transport within the region of our concern (θ between 320 and 340 K), and it avoids an unrealistic isentropic transport when the isentropes cross the orography.

Appendix B: Tracer Lifetime

The intention for using a 20-day exponential decaying tracer, T_{str}, in the CLaMS-2D run is to design a tracer that mimics the O_3 chemical evolution in the troposphere. In this appendix, we first discuss the representativeness

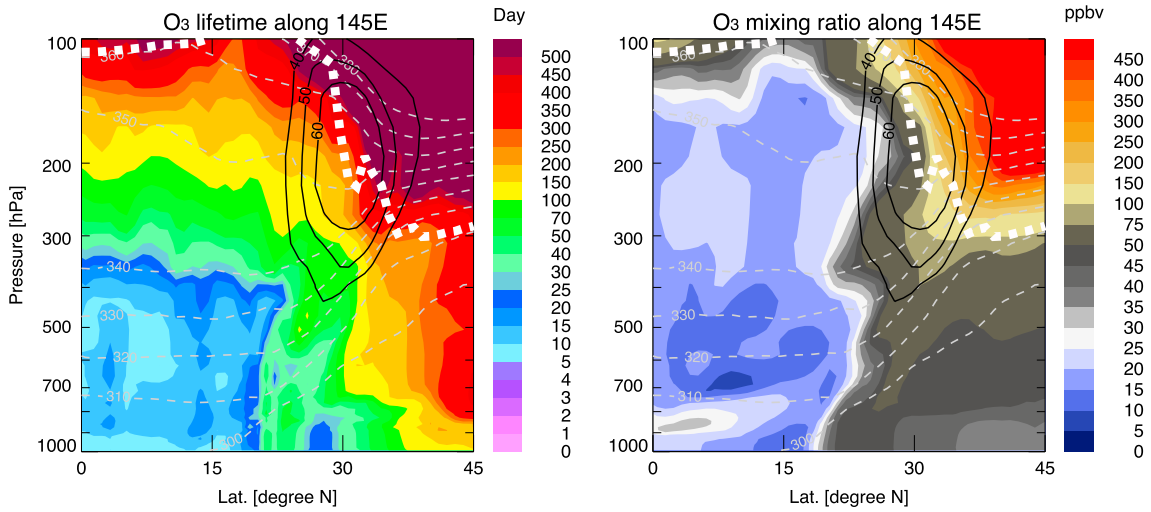

Figure B1. The cross section along 145°E of ozone lifetime (left) and of O_3 mixing ratios (right) with CAM-chem model on 23 January (1-day average). The dashed gray lines show the potential temperature. The black isolines show the zonal wind along 145°E. The white solid line shows thermal tropopause. CAM-chem = Community Atmospheric Model with chemistry, version 4.

of this tracer, followed by a discussion of the possible influence of this simplification on our quantification of stratospheric contributions.

Figure B1 shows an example of the lifetime distribution of O_3 based on the CAM-chem model, which indicates that the tropospheric lifetime of O_3 has a wide range from 400 days near the tropopause to 5 days in the deep tropics. O_3 is a long-lived tracer in midlatitude UTLS region, where O_3 has a representative lifetime ~100–200 days. The lifetime of O_3 is typically as short as 5–25 days in the deep tropics over the oceanic lower boundary, as shown in Figure B1. Therefore, the simplification of 20-day lifetime is a compromise of the large variation of the O_3 lifetime. And consequently, we cannot avoid the fact that decaying of T_{str} is too fast in the midlatitude, which possibly leads to an underestimation of the stratospheric contribution in the midlatitude and subtropics from our diagnosis. Meanwhile, we may also overestimate the stratospheric contribution over the oceanic convection-controlled region.

Figure B2 shows the cross section along 145°E of stratospheric tracer T_{str} with exponential decay of 10-, 20-, and 30-day lifetimes as well as the corresponding O_3S from the CAM-chem simulation. We first clarify some disagreements between the two models shown in this example. Note that no T_{str} above 15% is seen below 300 K isentrope in midlatitude from the CLaMS-2D run, which is mainly due to the lack of large-scale descending in CLaMS-2D. And we can also see all three tracers from CLaMS-2D underestimate the high values around 330 K between 30° and 30°N shown from CAM-chem simulation in the top left panel. This is related to the use of a constant lifetime in CLaMS artificial tracers, while the O_3 lifetime varies from 100 to 10 days for this region, as shown in the top panel of Figure B1. This approximation leads to underestimation of stratospheric influence where the O_3 lifetime is longer than the simulation setup. However, the aim of this work is not the accuracy of reproducing stratospheric O_3 mixing ratio but to diagnose the significance of the stratospheric contribution to the midtropospheric tropics. For this purpose, what we need is an artificial tracer that is capable of demonstrating the significance of stratospheric O_3 when it arrives at the midtropospheric tropics.

In section 4.1, we have clarified that the threshold ($T_{str} \geq 15\%$) is used to identify the significance of stratospheric contribution to the elevated O_3 layer in the midtroposphere. From the cross section of CAM-chem results (top panel in Figure B2), total O_3 mixing ratio ~40 ppbv (the dark gray contour in the top panel),the lower limit of secondary mode, contains ~20 ppbv stratospheric O_3 (O_3S) mixing ratio, which can be seen as a significant stratospheric contribution in this specific case. Thus, the tracer lifetime that we need should provide a similar distribution of $T_{str} \sim 15\%$, compared to the distribution of O_3S mixing ratio around 20 ppbv from the CAM-chem simulation. It is seen that the artificial tracer with a 20-day lifetime shows the best comparison with this quantity from the CAM-chem simulation. The 10-day tracer decreases too quickly from subtropics to tropics compared with CAM-chem. On the other hand, the 30-day tracer seems also comparable to CAM-chem O_3S in midtropospheric subtropics, but tracer values above 15% are observed around 10°N,

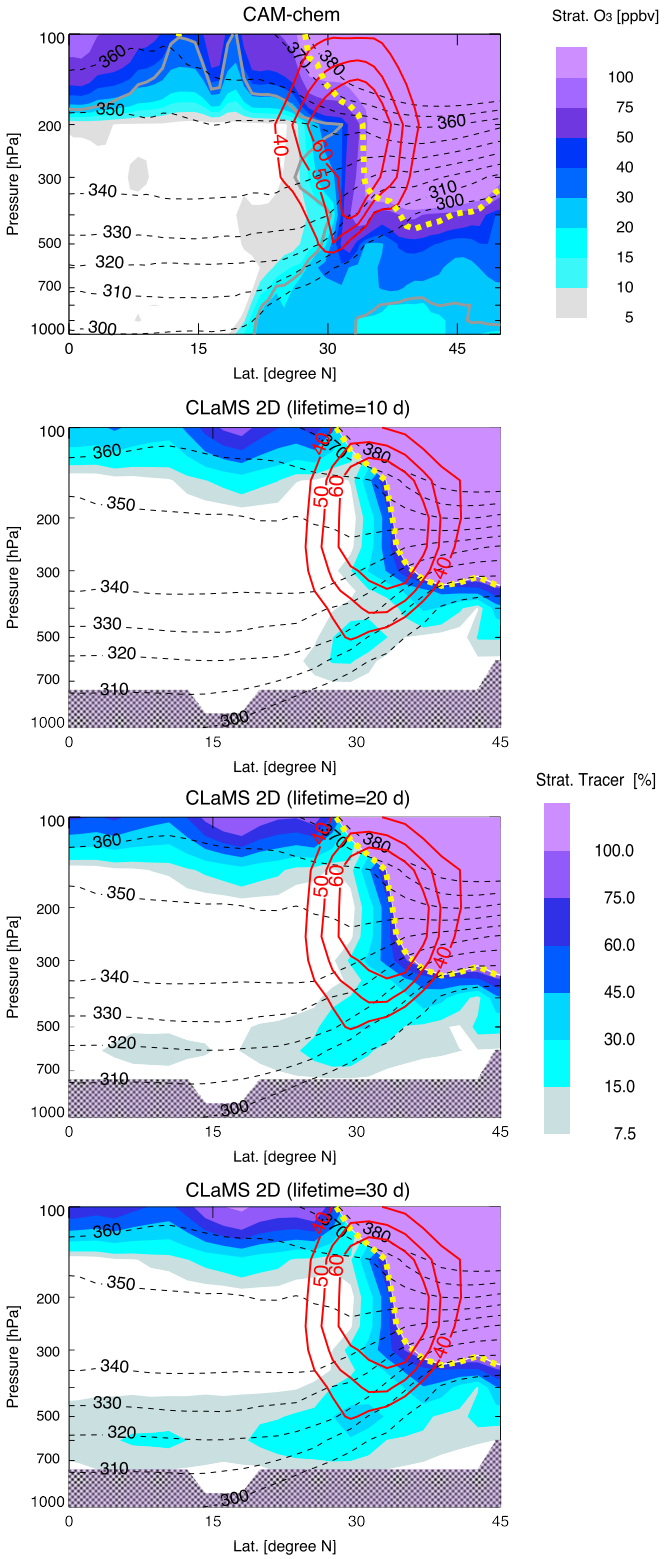

Figure B2. The cross section along 145°E of O_3S (unit in ppbv) on 23 January from the CAM-chem simulation (top) and T_{str} from CLaMS-2D with different *e*-folding times: 10, 20 and 30 days, respectively, from the second top panel to the bottom. The dark gray contour in the top panel shows the 40-ppbv isoline of total ozone from the CAM-chem simulation. CAM-chem = Community Atmospheric Model with chemistry, version 4; CLaMS-2D = Two-Dimensional Chemical Lagrangian Model of the Stratosphere.

which is inconsistent with the $O_3S \sim 20$ ppb from the CAM-chem result. The 30-day tracer throughout the whole simulation period shows better comparison with CAM-chem especially in the outer tropics and subtropics, which confirms that the O_3 lifetime in this region is mostly longer than 20 days. The 20-day tracer is a conservative choice in the study as to mimic the general O_3 loss rates in order to avoid overestimation of stratospheric significant influence in the deep tropics, especially the region controlled by oceanic convection.

Acknowledgments
We thank the CONTRAST team including pilots, technicians, forecasters, and scientists on the aircraft and on the ground for making the campaign a success and resulting the measurements that enabled this study. CONTRAST was funded by the National Science Foundation (NSF). CAM-chem is a component of NCAR's CESM1, which is supported by the NSF and the Office of Science of the U.S. Department of Energy. Computing resources were provided by NCAR's Climate Simulation Laboratory, sponsored by NSF and other agencies. This research was enabled by the computational and storage resources of NCAR's Computational and Information Systems Laboratory (CISL). Mengchu Tao thanks the NCAR visitor program for supporting her visit to NCAR where the work was conceptually formulated and most analyses completed. NCAR is funded by the NSF. We thank Frank Flocke for his helpful discussion and Elliot Atlas for his language advices. All the data used are listed in the references or publicly available. CONTRAST data can be obtained at http://data.eol.ucar.edu/master_list/?project=CONTRAST and model results can be obtained at https://fz-juelich.sciebo.de/s/srZ8uUakuU1koFX.

References

Alvarado, M., Logan, J., Mao, J., Apel, E., Riemer, D., Blake, D., et al. (2010). Nitrogen oxides and PAN in plumes from boreal fires during ARCTAS-B and their impact on ozone: An integrated analysis of aircraft and satellite observations. *Atmospheric Chemistry and Physics*, *10*(20), 9739–9760.

Anderson, D. C., Nicely, J. M., Salawitch, R. J., Canty, T. P., Dickerson, R. R., Hanisco, T. F., et al. (2016). A pervasive role for biomass burning in tropical high ozone/low water structures. *Nature Communications*, *7*, 10267.

Apel, E., Hornbrook, R., Hills, A., Blake, N., Barth, M., Weinheimer, A., et al. (2015). Upper tropospheric ozone production from lightning NO_x-impacted convection: Smoke ingestion case study from the DC3 campaign. *Journal of Geophysical Research: Atmospheres*, *120*, 2505–2523. https://doi.org/10.1002/2014JD022121

Bowman, K. P., Pan, L. L., Campos, T., & Gao, R. S. (2007). Observations of fine-scale transport structure in the upper troposphere from the high-performance instrument airborne platform for environmental research. *Journal of Geophysical Research*, *112*, D18111. https://doi.org/10.1029/2007JD008685

Brasseur, G. P., Orlando, J. J., & Tyndall, G. S. (Eds.) (1999). *Atmospheric Chemistry and Global Change*. New York: Oxford University Press.

Cau, P., Methven, J., & Hoskins, B. (2005). Representation of dry tropical layers and their origins in ERA-40 data. *Journal of Geophysical Research*, *110*(D6), D06110. https://doi.org/10.1029/2004JD004928

Cau, P., Methven, J., & Hoskins, B. (2007). Origins of dry air in the tropics and subtropics. *Journal of Climate*, *20*(12), 2745–2759.

Cooper, O. R., Parrish, D., Ziemke, J., Balashov, N., Cupeiro, M., Galbally, I., et al. (2014). Global distribution and trends of tropospheric ozone: An observation-based review. *Elementa: Science of the Anthropocene*, *2*(1), 000029. https://doi.org/10.12952/journal.elementa.000029

Dee, D. P., Uppala, S. M., Simmons, A. J., Berrisford, P., Poli, P., Kobayashi, S., et al. (2011). The ERA-interim reanalysis: Configuration and performance of the data assimilation system. *Quarterly Journal of the Royal Meteorological Society*, *137*, 553–597. https://doi.org/10.1002/qj.828

Emmons, L., Hess, P., Klonecki, A., Tie, X., Horowitz, L., Lamarque, J.-F., et al. (2003). Budget of tropospheric ozone during TOPSE from two chemical transport models. *Journal of Geophysical Research*, *108*(D8), 8372. https://doi.org/10.1029/2002JD002665

Fernandez, R., Salawitch, R., Kinnison, D., Lamarque, J.-F., & Saiz-Lopez, A. (2014). Bromine partitioning in the tropical tropopause layer: Implications for stratospheric injection. *Atmospheric Chemistry and Physics*, *14*(24), 13,391–13,410.

Fischer, H., Wienhold, F. G., Hoor, P., Bujok, O., Schiller, C., Siegmund, P., et al. (2000). Tracer correlations in the northern high latitude lowermost stratosphere: Influence of cross-tropopause mass exchange. *Geophysical Research Letters*, *27*(1), 97–100. https://doi.org/10.1029/1999GL010879

Folkins, I., Loewenstein, M., Podolske, J., Oltmans, S. J., & Proffitt, M. (1999). A barrier to vertical mixing at 14 km in the tropics: Evidence from ozonesondes and aircraft measurements. *Geophysical Research Letters*, *104*, 22,095–22,102.

Gregory, G., Westberg, D., Shipham, M., Blake, D., Newell, R., Fuelberg, H., et al. (1999). Chemical characteristics of Pacific tropospheric air in the region of the Intertropical Convergence Zone and South Pacific Convergence Zone. *Journal of Geophysical Research*, *104*(D5), 5677–5696.

Harris, J. M., & Oltmans, S. J. (1997). Variations in tropospheric ozone related to transport at American Samoa. *Journal of Geophysical Research*, *102*(D7), 8781–8791.

Hayashi, H., Kita, K., & Taguchi, S. (2008). Ozone-enhanced layers in the troposphere over the equatorial Pacific Ocean and the influence of transport of midlatitude UT/LS air. *Atmospheric Chemistry and Physics*, *8*(10), 2609–2621.

Hoor, P., Fischer, H., Lange, L., Lelieveld, J., & Brunner, D. (2002). Seasonal variations of a mixing layer in the lowermost stratosphere as identified by the CO-O_3 correlation from in situ measurements. *Journal of Geophysical Research*, *107*(D5), 4044. https://doi.org/10.1029/2000JD000289

Hoppe, C. M., Hoffmann, L., Konopka, P., Grooß, J.-U., Ploeger, F., Günther, G., et al. (2014). The implementation of the CLaMS lagrangian transport core into the chemistry climate model EMAC 2.40.1: Application on age of air and transport of long-lived trace species. *Geoscientific Model Development*, *7*(6), 2639–2651.

Hornbrook, R., Blake, D., Diskin, G., Fried, A., Fuelberg, H., Meinardi, S., et al. (2011). Observations of nonmethane organic compounds during ARCTAS-Part 1: Biomass burning emissions and plume enhancements. *Atmospheric Chemistry and Physics*, *11*(21), 11,103–11,130.

Jaffe, D. A., & Wigder, N. L. (2012). Ozone production from wildfires: A critical review. *Atmospheric Environment*, *51*, 1–10.

Khosrawi, F., Grooß, J.-U., Müller, R., Konopka, P., Kouker, W., Ruhnke, R., et al. (2005). Intercomparison between Lagrangian and Eulerian simulations of the development of mid-latitude streamers as observed by CRISTA. *Atmospheric Chemistry and Physics*, *5*(1), 85–95.

Kinnison, D. E., Brasseur, G. P., Walters, S., Garcia, R. R., Sassi, D. R. M. F., Harvey, V. L., et al. (2007). Sensitivity of chemical tracers to meteorological parameters in the MOZART-3 chemical transport model. https://doi.org/10.1029/2006JD007879

Kita, K., Kawakami, S., Miyazaki, Y., Higashi, Y., Kondo, Y., Nishi, N., et al. (2002). Photochemical production of ozone in the upper troposphere in association with cumulus convection over Indonesia. *Journal of Geophysical Research*, *107*(D3), 8400. https://doi.org/10.1029/2001JD000844

Kondo, Y., Koike, M., Kita, K., Ikeda, H., Takegawa, N., Kawakami, S., et al. (2002). Effects of biomass burning, lightning, and convection on O_3, CO, and NO_y over the tropical Pacific and Australia in August–October 1998 and 1999. *Journal of Geophysical Research*, *107*(D3), 8402. https://doi.org/10.1029/2001JD000820

Konopka, P., & Pan, L. L. (2012). On the mixing-driven formation of the Extratropical Transition Layer (ExTL). *Journal of Geophysical Research*, *117*, D18301. https://doi.org/10.1029/2012JD017876

Konopka, P., Steinhorst, H.-M., Grooß, J.-U., Günther, G., Müller, R., Elkins, J. W., et al. (2004). Mixing and ozone loss in the 1999–2000 Arctic vortex: Simulations with the 3-dimensional chemical Lagrangian Model of the Stratosphere (CLaMS). *Journal of Geophysical Research*, *109*, D02315. https://doi.org/10.1029/2003JD003792

Kunz, A., Konopka, P., Müller, R., & Pan, L. L. (2011). Dynamical tropopause based on isentropic potential vorticity gradients. *Journal of Geophysical Research*, *116*, D01110. https://doi.org/10.1029/2010JD014343

Lamarque, J.-F., Emmons, L., Hess, P., Kinnison, D. E., Tilmes, S., Vitt, F., et al. (2012). CAM-chem: Description and evaluation of interactive atmospheric chemistry in the Community Earth System Model. *Geoscientific Model Development*, *5*(2), 369–411.

Legras, B., Pisso, I., Berthet, G., & Lefevre, F. (2005). Variability of the Lagrangian turbulent diffusion in the lower stratosphere. *Atmospheric Chemistry and Physics*, *5*, 1605–1622.
Mahowald, N. M., Plumb, R. A., Rasch, P. J., del Corral, J., Sassi, F., & Heres, W. (2002). Stratospheric transport in a three-dimensional isentropic coordinate model. *Journal of Geophysical Research*, *107*(D15), 4254. https://doi.org/10.1029/2001JD001313
Mapes, B. E., & Zuidema, P. (1996). Radiative-dynamical consequences of dry tongues in the tropical troposphere. *Journal of the Atmospheric Sciences*, *53*(4), 620–638.
McKenna, D. S., Konopka, P., Grooß, J.-U., Günther, G., Müller, R., Spang, R., et al. (2002). A new Chemical Lagrangian Model of the Stratosphere (CLaMS): 1. Formulation of advection and mixing. *Journal of Geophysical Research*, *107*(D16), 4309. https://doi.org/10.1029/2000JD000114
Monks, P. S., Archibald, A., Colette, A., Cooper, O., Coyle, M., Derwent, R., et al. (2015). Tropospheric ozone and its precursors from the urban to the global scale from air quality to short-lived climate forcer. *Atmospheric Chemistry and Physics*, *15*(15), 8889–8973.
Newell, R. E., Thouret, V., Cho, J. Y. N., Stoller, P., Marenco, A., & Smit, H. G. (1999). Ubiquity of quasi-horizontal layers in the troposphere. *Nature*, *398*, 316–319.
Nicely, J. M., Anderson, D. C., Canty, T. P., Salawitch, R. J., Wolfe, G. M., Apel, E. C., et al. (2016). An observationally constrained evaluation of the oxidative capacity in the tropical western Pacific troposphere. *Journal of Geophysical Research: Atmospheres*, *121*, 7461–7488. https://doi.org/10.1002/2016JD025067
Oltmans, S. J., Johnson, B. J., Harris, J. M., Vömel, H., Thompson, A. M., Koshy, K., et al. (2001). Ozone in the Pacific tropical troposphere from ozonesonde observations. *Journal of Geophysical Research*, *106*(D23), 32,503–32,525.
Ordóñez, C., Lamarque, J.-F., Tilmes, S., Kinnison, D. E., Atlas, E. L., Blake, D. R., et al. (2012). Bromine and iodine chemistry in a global chemistry-climate model: Description and evaluation of very short-lived oceanic sources. *Atmospheric Chemistry and Physics*, *12*(3), 1423–1447.
Palmer, P. I., Parrington, M., Lee, J. D., Lewis, A. C., Rickard, A., Bernath, P. F., et al. (2013). Quantifying the impact of BOReal forest fires on Tropospheric oxidants over the Atlantic using Aircraft and Satellites (BORTAS) experiment: Design, execution and science overview. *Atmospheric Chemistry and Physics*, *13*(13), 6239–6261.
Pan, L. L., Atlas, E. L., Salawitch, R., Honomichl, S. B., Bresch, J. F., Randel, W. J., et al. (2017). The convective transport of active species in the tropics (CONTRAST) experiment. *Bulletin of the American Meteorological Society*, *98*(1), 106–128.
Pan, L. L., Honomichl, S. B., Randel, W. J., Apel, E. C., Atlas, E. L., Beaton, S. P., et al. (2015). Bimodal distribution of free tropospheric ozone over the tropical western Pacific revealed by airborne observations. *Geophysical Research Letters*, *42*, 7844–7851. https://doi.org/10.1002/2015GL065562
Pan, L. L., Konopka, P., & Browell, E. V. (2006). Observations and model simulations of mixing near the extratropical tropopause. *Journal of Geophysical Research*, *111*, D05106. https://doi.org/10.1029/2005JD006480
Parsons, D., Dabberdt, W., Cole, H., Hock, T., Martin, C., Barrett, A.-L., et al. (1994). The integrated sounding system: Description and preliminary observations from TOGA COARE. *Bulletin of the American Meteorological Society*, *75*(4), 553–567.
Pierrehumbert, R. T., & Yang, H. (1993). Global chaotic mixing on isentropic surfaces. *Journal of the Atmospheric Sciences*, *50*, 2462–2480.
Ploeger, F., Konopka, P., Günther, G., Grooß, J.-U., & Müller, R. (2010). Impact of the vertical velocity scheme on modeling transport across the tropical tropopause layer. *Journal of Geophysical Research*, *115*, D03301. https://doi.org/10.1029/2009JD012023
Postel, G. A., & Hitchman, M. H. (1999). A climatology of Rossby wave breaking along the subtropical tropopause. *Journal of the Atmospheric Sciences*, *56*, 359–373.
Randel, W. J., Rivoire, L., Pan, L. L., & Honomichl, S. B. (2016). Dry layers in the tropical troposphere observed during CONTRAST and global behavior from GFS analyses. *Journal of Geophysical Research: Atmospheres*, *121*, 14,142–14,158. https://doi.org/10.1002/2016JD025841
Rex, M., Wohltmann, I., Ridder, T., Lehmann, R., Rosenlof, K., Wennberg, P., et al. (2014). A tropical west Pacific OH minimum and implications for stratospheric composition. *Atmospheric Chemistry and Physics*, *14*(9), 4827–4841.
Rienecker, M., Suarez, M., Todling, R., Bacmeister, J., Takacs, L., & Liu, H. (2008). The GEOS-5 data assimilation system-documentation of versions 5.0. 1, 5.1. 0, and 5.2. 0, NASA technical report series on global modeling and data assimilation, v27, nASA/TM-2008-104606.
Roelofs, G.-J., & Lelieveld, J. (1997). Model study of the influence of cross-tropopause O_3 transports on tropospheric O_3 levels. *Tellus B: Chemical and Physical Meteorology*, *49*(1), 38–55.
Saiz-Lopez, A., Fernandez, R., Ordóñez, C., Kinnison, D., Gómez Martín, J. C., Lamarque, J.-F., & Tilmes, S. (2014). Iodine chemistry in the troposphere and its effect on ozone. *Atmospheric Chemistry and Physics*, *14*(23), 13,119–13,143.
Scott, R., & Cammas, J.-P. (2002). Wave breaking and mixing at the subtropical tropopause. *Journal of the Atmospheric Sciences*, *28*, 2347–2361.
Shindell, D., & Faluvegi, G. (2009). Climate response to regional radiative forcing during the twentieth century. *Nature Geoscience*, *2*(4), 294–300.
Singh, H., Anderson, B., Brune, W., Cai, C., Cohen, R., Crawford, J., et al. (2010). Pollution influences on atmospheric composition and chemistry at high northern latitudes: Boreal and California forest fire emissions. *Atmospheric Environment*, *44*(36), 4553–4564.
Singh, H. B., Salas, L., Herlth, D., Kolyer, R., Czech, E., Viezee, W., et al. (2003). In situ measurements of HCN and CH_3CN over the Pacific Ocean: Sources, sinks, and budgets. *Journal of Geophysical Research*, *108*, 8795. https://doi.org/10.1029/2002JD003006
Singh, H., Viezee, W., Chen, Y., Bradshaw, J., Sandholm, S., Blake, D., et al. (2000). Biomass burning influences on the composition of the remote south Pacific troposphere: Analysis based on observations from PEM-Tropics-A. *Atmospheric Environment*, *34*(4), 635–644.
Stevenson, D. S., Dentener, F. J., Schultz, M. G., Ellingsen, K., van Noije, T. P. C., Wild, O., et al. (2006). Multimodel ensemble simulations of present-day and near-future tropospheric ozone. *Journal of Geophysical Research*, *111*, D08301. https://doi.org/10.1029/2005JD006338
Stevenson, D. S., Young, P., Naik, V., Lamarque, J.-F., Shindell, D. T., Voulgarakis, A., et al. (2013). Tropospheric ozone changes, radiative forcing and attribution to emissions in the Atmospheric Chemistry and Climate Model Intercomparison Project (ACCMIP). *Atmospheric Chemistry and Physics*, *13*(6), 3063–3085.
Stocker, T. (Ed.) (2014). *Climate Change 2013: The physical science basis: Working Group I Contribution to the Fifth Assessment Report of the Intergovernmental Panel on Climate Change*. Cambridge, UK and New York: Cambridge University Press.
Stohl, A., Forster, C., Frank, A., Seibert, P., & Wotawa, G. (2005). Technical note: The Lagrangian particle dispersion model FLEXPART version 6.2. *Atmospheric Chemistry and Physics*, *5*, 2461–2474.
Thompson, A. M., Oltmans, S. J., Tarasick, D. W., von der Gathen, P., Smit, H. G., & Witte, J. C. (2011). Strategic ozone sounding networks: Review of design and accomplishments. *Atmospheric Environment*, *45*(13), 2145–2163.
Thouret, V., Cho, J. Y. N., Evans, M. J., Newell, R. E., Avery, M. A., Barrick, J. D. W., et al. (2001). Tropospheric ozone layers observed during PEM-Tropics B. *Journal of Geophysical Research*, *106*(D23), 32,527–32,538.
Tilmes, S., Lamarque, J.-F., Emmons, L. K., Kinnison, D. E., Marsh, D., Garcia, R. R., et al. (2016). Representation of the Community Earth System Model (CESM1) CAM4-chem within the Chemistry-climate model initiative (CCMI). *Geoscientific Model Development*, *9*, 1853–1890.

Vogel, B., Pan, L. L., Konopka, P., Günther, G., Müller, R., Campos, T., et al. (2011). Transport pathways and signatures of mixing in the extratropical tropopause region derived from Lagrangian model simulations. *Journal of Geophysical Research*, *116*, D05306. https://doi.org/10.1029/2010JD014876

Wang, Y., Jacob, D. J., & Logan, J. A. (1998). Global simulation of tropospheric O_3-NO_x-hydrocarbon chemistry: 3. Origin of tropospheric ozone and effects of nonmethane hydrocarbons. *Journal of Geophysical Research*, *103*(D9), 10,757–10,767.

Waugh, D. W., & Polvani, L. M. (2000). Climatology of intrusions into the tropical upper troposphere. *Geophysical Research Letters*, *27*(23), 3857–3860.

Yoneyama, K., & Parsons, D. B. (1999). A proposed mechanism for the intrusion of dry air into the tropical western Pacific region. *Journal of the Atmospheric Sciences*, *56*(11), 1524–1546.

Young, P., Archibald, A., Bowman, K., Lamarque, J.-F., Naik, V., Stevenson, D., et al. (2013). Pre-industrial to end 21st century projections of tropospheric ozone from the Atmospheric chemistry and climate model intercomparison project (ACCMIP). *Atmospheric Chemistry and Physics*, *13*(4), 2063–2090.